Primordial compositions of refractory inclusions

L. Grossman [a,f,*], S.B. Simon [a], V.K. Rai [b,1], M.H. Thiemens [b], I.D. Hutcheon [c],
R.W. Williams [c], A. Galy [d], T. Ding [e], A.V. Fedkin [a], R.N. Clayton [a,f], T.K. Mayeda [f,†]

[a] Department of the Geophysical Sciences, The University of Chicago, 5734 S. Ellis Avenue, Chicago, IL 60637, USA
[b] Department of Chemistry and Biochemistry, University of California, San Diego, CA 92093-0352, USA
[c] Lawrence Livermore National Laboratory, Livermore, CA 94551-0808, USA
[d] Department of Earth Science, University of Cambridge, Cambridge CB2 3EQ, England, UK
[e] Institute of Mineral Resources, Chinese Academy of Geological Sciences, Beijing 100037, China
[f] Enrico Fermi Institute, The University of Chicago, Chicago, IL 60637, USA

Abstract

Bulk chemical and O-, Mg- and Si-isotopic compositions were measured for each of 17 Types A and B refractory inclusions from CV3 chondrites. After bulk chemical compositions were corrected for non-representative sampling in the laboratory, the Mg- and Si-isotopic compositions of each inclusion were used to calculate its original chemical composition assuming that the heavy-isotope enrichments of these elements are due to Rayleigh fractionation that accompanied their evaporation from CMAS liquids. The resulting pre-evaporation chemical compositions are consistent with those predicted by equilibrium thermodynamic calculations for high-temperature nebular condensates, but only if different inclusions condensed from nebular regions that ranged in total pressure from 10^{-6} to 10^{-1} bar, regardless of whether they formed in a system of solar composition or in one enriched in dust of ordinary chondrite composition relative to gas by a factor of 10 compared to solar composition. This is similar to the range of total pressures predicted by dynamic models of the solar nebula for regions whose temperatures are in the range of silicate condensation temperatures. Alternatively, if departure from equilibrium condensation and/or non-representative sampling of condensates in the nebula occurred, the inferred range of total pressure could be smaller. Simple kinetic modeling of evaporation successfully reproduces observed chemical compositions of most inclusions from their inferred pre-evaporation compositions, suggesting that closed-system isotopic exchange processes did not have a significant effect on their isotopic compositions. Comparison of pre-evaporation compositions with observed ones indicates that 80% of the enrichment in refractory $CaO + Al_2O_3$ relative to more volatile $MgO + SiO_2$ is due to initial condensation and 20% due to subsequent evaporation for both Types A and B inclusions.
© 2008 Elsevier Ltd. All rights reserved.

1. INTRODUCTION

Whether calcium-, aluminum-rich inclusions (CAIs) in CV3 chondrites are solar nebular condensates or evaporation residues has been debated since the earliest days of research on these objects, with Christophe Michel-Lévy (1968) and Grossman (1972) suggesting that they are condensates and Chou et al. (1976) and Notsu et al. (1978) arguing that they are residues. Grossman et al. (2000) seemed to provide the answer to this important question when they argued that they are actually both. They noted that major element bulk compositions of coarse-grained inclusions, when corrected for non-representative sampling in the laboratory, are deficient in MgO and SiO_2 compared to those predicted by thermodynamic calculations for high-temperature, solar nebular condensates, and that enrichments in the heavy isotopes of Mg and Si reported for such inclusions, when interpreted as being due to partial evapo-

ration of these oxides, can account approximately for the magnitudes of these deficits. Thus, Grossman et al. (2000) concluded that the major element compositions of these objects resulted from high-temperature condensation of refractory assemblages, followed by evaporation of several tens of percent of the Mg and Si from them during partial melting in a hydrogen-rich gas.

In that work, the chemical compositions were determined for one group of inclusions, and the isotopic compositions for another. If, instead, both the present chemical composition and the Mg- and Si-isotopic compositions were known for any one inclusion, the bulk composition of its precursor could be determined by peeling away the effects of evaporation. Furthermore, if the precursor compositions were known for each of a suite of inclusions, comparisons with predictions of condensation models could be used to draw inferences about how representatively each object sampled solar nebular condensates, the total pressure and dust/gas ratio of the system from which the inclusions condensed and the temperatures at which they became chemically isolated from the gas. This paper presents the results of such a study. Preliminary versions of this work were given by Simon et al. (2004) and Grossman et al. (2007).

2. ANALYTICAL TECHNIQUES

2.1. Sampling

Relatively large, coarse-grained, white inclusions were located on slab surfaces of the Allende, Efremovka, Leoville and Vigarano CV3 chondrites. Those selected ranged from 2 mm to more than 1 cm in shortest dimension, and, based on their rounded outlines, appeared to be complete, unfragmented individuals. Material was excavated from each one using stainless steel dental tools. Only small portions of each inclusion were sampled, as excavations were deliberately shallow and avoided inclusion edges in order to prevent contamination with adjacent matrix. Excavated material was ground into a powder and homogenized for 30 min with an agate mortar and pestle. For the present work, each powdered sample, weighing from 5 to 200 mg but most ~40 mg, was scooped into separate portions for major element chemical analysis, Mg-isotopic analysis, and O- and Si-isotopic analyses. Aliquots of three of the samples were also used for U–Pb age determinations by Amelin et al. (2002). In most, but not all, cases, the mirror image of each inclusion on a facing slab was made into one or more polished thin sections.

2.2. Major element chemical analysis

A bulk chemical analysis was obtained for each sample by modal recombination of spot analyses of mineral phases in the thin section(s) or by instrumental neutron activation analysis (INAA) of one of the aliquots or by both methods. In our modal recombination technique, quantitative wavelength-dispersive analyses were obtained with a Cameca SX-50 electron microprobe operated at 15 kV and a beam current of 50 nA. Analyses were collected along regularly-spaced, linear traverses from rim to rim across inclusions.

These data yielded average phase compositions and relative abundances from which bulk compositions were calculated. The CaO/Al_2O_3 ratios of compositions obtained in this way more consistently approach the solar value than do those obtained by INAA. Because we assume that actual bulk compositions of CAIs have solar CaO/Al_2O_3 ratios, the modal recombination method was preferred. Further details of the techniques employed and of our reasons for preferring modal recombination data were given in Simon and Grossman (2004).

2.3. Magnesium-isotopic analysis

At Lawrence Livermore National Laboratory (LLNL), samples were dissolved in an HNO_3–HF–$HClO_4$ acid solution at ~100 °C in sealed PFA Teflon vials, taken to dryness and then digested a second time in an HCl–HF–$HClO_4$ acid solution. The samples were dried again, converted to nitrate with HNO_3 and finally redissolved in 1 M HNO_3. Insoluble residues (spinel + perovskite) were separated by centrifugation. Mg was purified from the dissolved fraction on AG50W-X8 (200–400 mesh) resin columns with quantitative recovery. The Mg isotope compositions were measured with the LLNL IsoProbe multi-collector, magnetic sector ICP-MS, using static multi-collection. Mg isotope compositions are reported as $\delta^{25}Mg$ and $\delta^{26}Mg$, determined with the standard–sample–standard bracketing technique and calculated relative to the DSM3 Mg metal standard (Galy et al., 2003). The purified Mg from each CAI was analyzed at least three times, and the uncertainties quoted are two standard deviations of the mean. The average reproducibility for these measurements is 0.15‰ and 0.40‰ for $\delta^{25}Mg$ and $\delta^{26}Mg$, respectively.

At Cambridge University, methods of chemical digestion, Mg separation and measurement of Mg-isotopic composition were similar to those used by Galy et al. (2000). The samples were powdered and digested in HNO_3–HF–$HClO_4$ acid solution at ~140 °C in sealed PFA Teflon® vials, taken to dryness and then digested a second time in an HCl–HNO_3 acid solution. The samples were dried again, converted to chloride with HCl and finally redissolved in 3 M HCl. Mg was separated from Al and Fe by co-precipitation of the latter with NH_3 at pH $\leqslant 7$, and purified of other elements on AG50W-X12 cation exchange resin with quantitative recovery (Tipper et al., 2006). The Mg-isotopic compositions were measured with a Nu-instruments multi-collector, magnetic sector ICP-MS, using static multi-collection (Galy et al., 2001) and reported in an identical manner as the measurements performed at LLNL. Each sample underwent at least duplicate mass spectrometric analysis, and the uncertainties quoted are two standard deviations of the mean. The average reproducibility for these measurements is 0.07‰ and 0.13‰ for $\delta^{25}Mg$ and $\delta^{26}Mg$, respectively, and compares favorably to the long-term total procedural precision on $\delta^{25}Mg$ of 0.07‰ (Tipper et al., 2006).

2.4. Oxygen- and silicon-isotopic analysis

At the University of Chicago, reaction of silicates and oxides with bromine pentafluoride (BrF_5) gave quantitative

yields of both oxygen (as O_2) and silicon (as SiF_4). Oxygen was purified using 13× molecular sieve as in Clayton and Mayeda (1983). SiF_4 was purified by gas chromatography as in Molini-Velsko et al. (1986). Measurements of $\delta^{18}O$, $\delta^{17}O$, $\delta^{30}Si$ and $\delta^{29}Si$ were done with double-collecting mass spectrometers. The 1σ uncertainty on these data is ±0.2‰.

Some of the fluorinations and oxygen-isotopic analyses were performed at the University of California, San Diego (UCSD), using the following procedure. Nickel tubes were cleaned under high vacuum by heating and pumping at 400 °C overnight. A nickel tube was filled with dry nitrogen and placed in a dry box, together with a 1- to 3-mg powdered sample, where they were left for at least 6 h before the tube was opened and the sample powder loaded into it. The tube was reconnected to the extraction line and heated under vacuum at ~300 °C overnight. BrF_5 was added to the reaction tube, kept at room temperature for 6 h (in most cases) to remove adsorbed water, and pumped away. A new batch of BrF_5 was cleaned of non-condensable impurities by freezing at −90 °C, and then was added to the tube and heated to 700 °C for 36 h. The reaction products were passed through two liquid-nitrogen-cooled traps, and the O_2 was collected by freezing onto a molecular sieve. The oxygen-isotopic measurements were carried out on a Finnigan MAT-251 mass spectrometer. The cold-trap was warmed to −120 °C to evaporate SiF_4, which was transferred into a quarter-inch Pyrex tube. All the sealed tubes of SiF_4 were sent to the Institute of Mineral Resources of the Chinese Academy of Geological Sciences in Beijing for silicon-isotopic measurements. Several NBS-28 samples were processed in the same way as a check on the procedure.

In Beijing, additional NBS-28 samples were fluorinated by the procedure of Clayton and Mayeda (1963), after first separating CF_4, SiF_4 and SF_6 impurities from BrF_5 obtained from the Wuhan Institute of Chemical Products. Because of the different vapor pressures of these species, the impurities can be removed by multiple cycles of cryogenic vaporization and condensation using an ethanol–liquid nitrogen mixture (−70 °C). At this temperature, BrF_5 remains in the solid phase, but the impurities are present in the vapor phase and can be pumped to waste. A dry ice–acetone mixture (−80 °C) was used to extract the SiF_4 fluorination product from the BrF_5 reagent.

Silicon isotope measurements of samples and standards were carried out with a MAT-253 gas source isotope ratio mass spectrometer as described by Ding (2004) and Ding et al. (2005). A 9.12-kV accelerating voltage was used with a magnetic field intensity of 0.9509 T. Masses 85, 86 and 87 were collected simultaneously, and the results are expressed as $\delta^{29}Si$ and $\delta^{30}Si$ values relative to NBS-28. Six samples of NBS-28 that were fluorinated in San Diego were isotopically analyzed in Beijing against NBS-28 that was fluorinated in Beijing. The mean $\delta^{29}Si$ and $\delta^{30}Si$ were 0.019‰ and 0.037‰, respectively. Their 1σ standard deviations were ±0.092 and ±0.177, respectively, which include uncertainty due to blanks, fluorination, extraction and measurement. Thus, 1σ uncertainties of ±0.1 for $\delta^{29}Si$ and ±0.2 for $\delta^{30}Si$ were adopted for the meteorite samples.

3. RESULTS

3.1. Major element bulk compositions

As defined by Grossman (1980), coarse-grained, Ca- and Al-rich inclusions in CV3 chondrites are found in two mineralogical varieties. The primary phase assemblage of Type As consists of melilite (a solid solution between gehlenite ($Ca_2Al_2SiO_7$) and åkermanite ($Ca_2MgSi_2O_7$)), spinel ($MgAl_2O_4$), perovskite ($CaTiO_3$) and <35 vol % fassaite, a Ca-, Al-rich clinopyroxene rich in diopside ($CaMgSi_2O_6$) and containing both Ti^{3+} and Ti^{4+} (Dowty and Clark, 1973). These are further subdivided into "fluffy" and compact sub-types, the former much more irregularly-shaped and heavily altered than the latter. The primary phase assemblage of Type Bs consists of melilite, spinel, anorthite ($CaAl_2Si_2O_8$) and $\geqslant$35 vol % fassaite. These were subdivided by Wark and Lovering (1977) into B1s, which contain massive melilite mantles and B2s which do not.

Major element chemical data for ten of the inclusions used in the present study were given by Simon and Grossman (2004). For 1623-8, the INAA data of Sylvester et al. (1992) were used. Those for the compact Type A (CTA) inclusions, F11, TS32, E49 and E56; the Type B inclusion, TS34; and the unusual forsterite (Mg_2SiO_4)-bearing Type B, E60, are listed in Table 1. In the case of the INAA data for E60, the quoted errors in Table 1 are the 1σ uncertainties due only to counting statistics. For all inclusions whose compositions were determined by INAA (E13, E49A, E55, E60, E62 and 1623-8), SiO_2 was determined by difference. Consequently, the uncertainty in this oxide may be significantly underestimated by the quoted counting statistics due to the possible concentration of any systematic errors in determining all of the other elements. As found by Simon and Grossman (2004), the CTAs tend to have lower MgO and SiO_2 contents than Type Bs. The four CTAs measured in this study have 3–6 wt% MgO and 21–26 wt% SiO_2, whereas the single Type B analyzed here has 10.74 wt% MgO and 26.55 wt% SiO_2. The forsterite-bearing Type B, E60, contains much more MgO and SiO_2 than any Type A or B inclusion, consistent with its high modal abundance of forsterite.

3.2. Magnesium-isotopic compositions

The Livermore and Cambridge measurements of $\delta^{26}Mg$ and $\delta^{25}Mg$, with their 2σ uncertainties, are given in Table 2 for all samples in this study. The $\delta^{25}Mg$ data from the two laboratories are plotted against one another in Fig. 1, from which the excellent agreement between them is evident. Of the eight samples whose magnesium-isotopic data were measured in both laboratories, only two deviate significantly from the 1:1 line, TS33 slightly so and TS32 much more so. These differences are probably due to internal sample heterogeneity.

3.3. Oxygen-isotopic compositions

The Chicago and San Diego measurements of $\delta^{18}O$ and $\delta^{17}O$ are given in Table 2 for all samples in this study.

Table 1
Chemical compositions of inclusions used in this work and not previously published (wt% unless otherwise indicated)

Inclusion	TS32	F11	E49	E56	TS34	E60
Type	CTA	CTA	CTA	CTA	B1	Fo-bearing B
Meteorite	Allende	Allende	Efremovka	Efremovka	Allende	Efremovka
Method	MR[a]	MR	MR	MR	MR	INAA
Na_2O (ppm)	n.d.	n.d.	n.d.	n.d.	n.d.	640 ± 6
MgO	5.73	5.76	3.71	5.47	10.74	16.82 ± 0.06
Al_2O_3	28.88	31.16	31.34	37.47	32.23	18.49 ± 0.05
SiO_2	25.71	25.38	25.51	21.33	26.55	39.19^{b}
CaO	38.10	36.72	38.77	34.38	28.28	24.7 ± 0.1
TiO_2	1.58	0.98	0.67	1.36	2.20	0.42 ± 0.01
V_2O_3 (ppm)	n.d.	n.d.	n.d.	n.d.	n.d.	196 ± 1
MnO (ppm)	n.d.	n.d.	n.d.	n.d.	n.d.	19.2 ± 0.4
FeO (ppm)	n.d.	n.d.	n.d.	n.d.	n.d.	2973 ± 57

n.d., not determined.
[a] MR, modal recombination.
[b] By difference.

The data are plotted on the standard $\delta^{17}O$ vs $\delta^{18}O$, three-isotope plot in Fig. 2, along with the Terrestrial Fractionation (TF) line and the carbonaceous chondrite anhydrous mineral (CCAM) line, the latter defined by compositions of many bulk, anhydrous inclusions in carbonaceous chondrites and their mineral separates measured in Chicago (Clayton et al., 1977). Although the UCSD data scatter more widely about the CCAM line than the Chicago data, the points generally lie quite close to the CCAM line. There is no evidence that any of the inclusions in this study are FUN inclusions.

3.4. Silicon-isotopic compositions

The Beijing measurements of $\delta^{30}Si$ and $\delta^{29}Si$, and Chicago results for $\delta^{30}Si$, are given in Table 2. In Fig. 3, $\delta^{29}Si$ is plotted against $\delta^{30}Si$ for all samples used in this study for which both were measured, i.e., the Beijing data and samples F11, TS34 and F7 from Molini-Velsko (1983). The line shown is the average of the two least-squares regression lines through the Beijing data. It has a slope of 0.500 ± 0.001 and an intercept of 0.065 ± 0.003, indicating that the isotopic variations are dominated by mass-dependent fractionation and that no significant impurities of interfering masses survived the chemical procedure for SiF_4 separation. When the three data points from Molini-Velsko (1983) are included, the slope of the mean regression becomes 0.506 ± 0.002 and the intercept becomes 0.034 ± 0.005.

4. DISCUSSION

4.1. Major element bulk compositions corrected for sampling bias

Grossman et al. (2000) stressed the difficulty of obtaining representative analyses of refractory inclusions when sampling small fractions of them, and attempted to overcome this laboratory bias. They did so by assuming that every Type A and B CAI has a chondritic Ca/Al ratio,

and correcting published major element compositions of a suite of these objects by adding or subtracting spinel until this ratio was achieved. This approach was modified by Simon and Grossman (2004), who calculated a range of possible compositions for each object by computing how much spinel, melilite and fassaite, taken one at a time, had to be added to or subtracted from the bulk composition measured by modal recombination, in order to achieve a chondritic Ca/Al ratio. For each inclusion, a best estimate of the bulk composition was obtained by taking the mean of the separate corrected compositions.

Incorporated into the present work are six of the inclusions whose mean compositions were determined in this way by Simon and Grossman (2004). Added to these are another 11 inclusions: four whose chemical compositions were also reported by Simon and Grossman (2004) but which were measured by INAA, six whose chemical compositions were determined since that work and are shown in Table 1, and another, 1623-8, whose composition was taken from the literature. Among these additional eleven inclusions are five whose chemical compositions could be corrected for non-representative sampling as in Simon and Grossman (2004) because thin sections were available from which phase compositions could be determined and modal recombination performed.

Four of the remaining six inclusions are compact Type As, and E60 is a forsterite-bearing Type B. Because thin sections of these samples were not available, their chemical compositions were obtained by INAA. Melilite and fassaite are important phases in compact Type As, and each exhibits a wide range of solid solution compositions within a given inclusion. Because the modal recombination technique makes use of large numbers of analyses of each of these phases within each inclusion, corrected bulk compositions are based on very good estimates of the mean compositions of melilite and fassaite. For both of these minerals, the grand average was taken of the average composition obtained for each compact Type A inclusion, and is listed in Table 3. For those compact Type A inclusions whose compositions were measured by INAA, the data in Table 3 were

Table 2
Mg-, O-, and Si-isotopic compositions measured for this study (‰)

Sample	Meteorite	Incl. Type	δ^{26}Mg LLNL	δ^{25}Mg LLNL	δ^{26}Mg Camb.	δ^{25}Mg Camb.	δ^{18}O UCSD	δ^{17}O UCSD	δ^{18}O UC	δ^{17}O UC	δ^{30}Si Beijing	δ^{29}Si Beijing	δ^{30}Si UC
TS32	AL	CTA	18.29 ± 0.31	8.52 ± 0.20	16.18 ± 0.05	7.57 ± 0.05	—	—	−7.3	−11.0	2.42	1.29	2.52
E13	EF	CTA	−0.80 ± 0.06	−1.16 ± 0.05	−0.36 ± 0.22	−0.90 ± 0.11	—	—	−34.5	−37.4	—	—	−1.02
E49A	EF	CTA	—	—	5.79 ± 0.07	2.17 ± 0.05	−3.14 ± 0.08	−8.60 ± 0.17	—	—	1.62	0.82	—
E49	EF	CTA	11.94 ± 0.20	5.41 ± 0.07	—	—	−0.95 ± 0.06	−6.52 ± 0.05	—	—	2.30	1.17	—
E55	EF	CTA	—	—	5.09 ± 0.34	1.35 ± 0.23	−4.41 ± 0.08	−7.40 ± 0.06	—	—	3.74	1.95	—
E56	EF	CTA	7.34 ± 0.73	2.43 ± 0.19	7.27 ± 0.15	2.46 ± 0.10	−7.16 ± 0.02	−10.69 ± 0.03	—	—	1.66	0.81	—
E62	EF	CTA	3.42 ± 0.33	−1.25 ± 0.011	—	—	−7.86 ± 0.04	−12.40 ± 0.07	—	—	5.41	2.79	—
TS33	AL	B1	8.59 ± 0.15	3.83 ± 0.07	9.18 ± 0.13	4.19 ± 0.01	—	—	−19.4	−21.5	—	—	2.82
TS34	AL	B1	11.89 ± 0.52	5.63 ± 0.28	—	—	—	—	—	—	—	—	—
3537-2	LE	B1	7.54 ± 0.50	3.20 ± 0.27	7.56 ± 0.09	3.32 ± 0.08	—	—	−23.1	−27.3	—	—	2.56
F2 (TS65)	AL	B2	12.99 ± 0.10	6.11 ± 0.05	12.88 ± 0.08	6.12 ± 0.03	−15.98 ± 0.02	−19.12 ± 0.07	—	—	4.10	2.11	—
E107	EF	A/B	4.83 ± 0.15	1.86 ± 0.10	5.17 ± 0.16	2.12 ± 0.05	−10.18 ± 0.05	−14.38 ± 0.04	—	—	0.92	0.55	—
Golfball	AL	B	—	—	3.86 ± 0.11	1.61 ± 0.06	−22.10 ± 0.03	−25.70 ± 0.05	—	—	0.49	0.39	—
E60	EF	Fo-B	7.69 ± 0.35	3.78 ± 0.12	7.75 ± 0.07	3.78 ± 0.03	−21.06 ± 0.02	−24.77 ± 0.09	—	—	2.91	1.56	—

Stated uncertainties for Mg are 2σ. Uncertainties for Si-isotopic data are ±0.2‰ for δ^{29}Si and ±0.4‰ for δ^{30}Si (2σ). For the O-isotopic compositions, uncertainties on the UC data are <0.1‰, and the stated uncertainties for the UCSD data are 1σ. LLNL, Lawrence Livermore National Laboratory; Camb., Cambridge University; UCSD, University of California, San Diego; UC, University of Chicago; AL, Allende; EF, Efremovka; LE, Leoville.
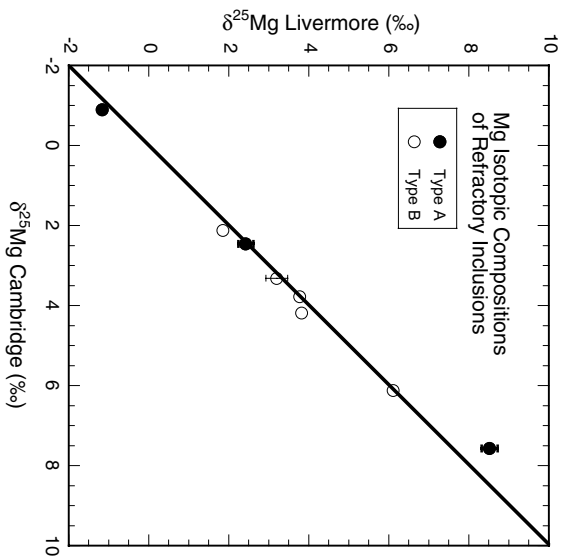

Fig. 1. Measurements of the Mg-isotopic compositions of CAIs performed in Livermore and in Cambridge are usually in excellent agreement with one another, but two samples (TS32 and TS33) appear to be internally heterogeneous. Two-σ uncertainties are shown when larger than the data points.
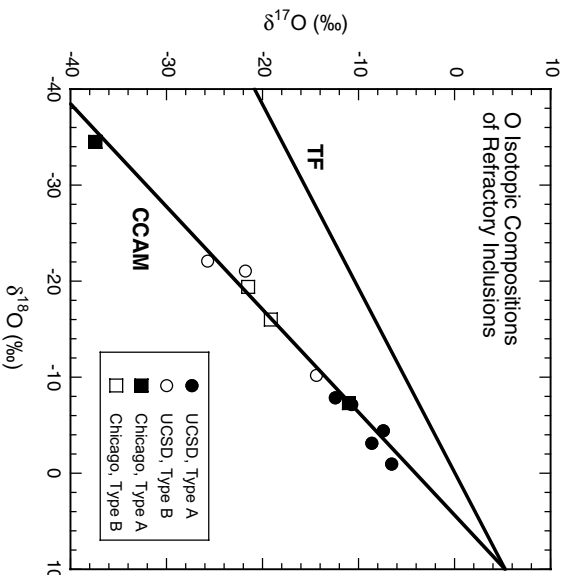

Fig. 2. Oxygen-isotopic data for CAIs measured in this work. All data plot very close to the CCAM line, indicating that there are no FUN inclusions among this suite of objects. Data points are larger than the 2σ error bars.

used to correct for non-representative sampling. Because the sampling corrections are not based on mineral analyses from the same inclusions, this procedure may introduce yet another source of uncertainty beyond that expressed by the formal error bars for those inclusions whose compositions were measured by INAA. Since the average melilite and fassaite compositions are not well-known for forsterite-bearing CAIs, the sampling correction for E60 was based only on spinel. In the case of 1623-8, the sixth CAI for
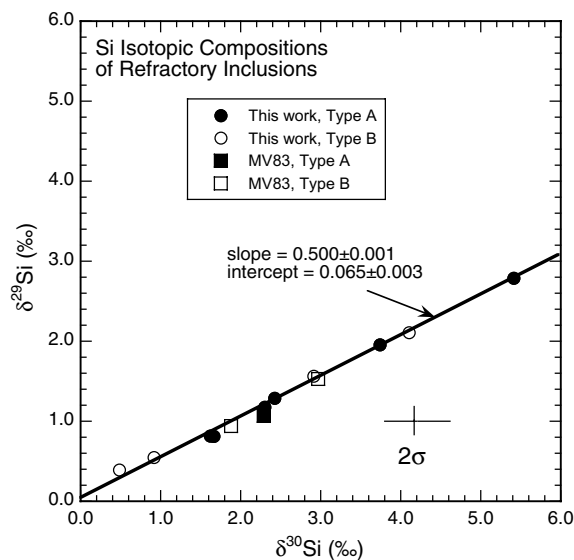
Fig. 3. $\delta^{29}Si$ vs $\delta^{30}Si$, relative to NBS-28, of all inclusions in this study for which both were measured. The line drawn has the mean slope and intercept of the two least-squares regression lines through the new measurements (filled circles), whose typical 1σ error bars are also shown. Some data from Molini-Velsko (1983); labeled MV83 were also used here.

Table 3
Average compositions of melilite and fassaite in compact Type A inclusions

	Melilite	SD	Fassaite	SD
MgO	3.37	1.05	6.70	0.66
Al_2O_3	28.69	2.66	20.27	2.11
SiO_2	26.86	1.51	32.48	1.31
CaO	40.99	0.42	24.86	0.28
TiO_2	0.07	0.04	15.78	2.18
No. of inclusions	8		5	

SD, standard deviation.

which a composition determination by INAA was used here, another estimate of its chemical composition made by modal recombination (MacPherson and Davis, 1993) gave grossly different results, and was rejected. Nevertheless, mineral compositions from the same thin section used for the modal recombination were used for the sampling corrections to the INAA data.

The best estimate of the major element composition of each of the inclusions investigated in this work, after renormalization to 100% $CaO + MgO + Al_2O_3 + SiO_2$ (CMAS), is listed on Table 4.

4.2. Condensation paths for systems of solar composition

Equilibrium condensation calculations were performed at 2 K temperature intervals at discrete total pressures between 10^{-1} and 10^{-7} bar, using the VAPORS program of Ebel and Grossman (2000), the thermodynamic data and solution models therein, and updated solar system abundance data for O, C and S that were discussed and em-

ployed by Fedkin and Grossman (2006). The bulk chemical composition of the TiO_2- and metal-free condensate assemblage was calculated at each temperature step. "Condensation paths" are simply curves connecting bulk chemical compositions calculated at successive temperature steps. Over the temperature range where calculated bulk compositions are closest to those observed for CAIs, a condensation path for MgO and SiO_2 is shown in Fig. 4a for each of several different, relatively low values of total pressure, P^{tot}. Because of significant overlaps, paths for relatively high P^{tot} are shown in a separate figure, Fig. 4b, for clarity. Because Ca and Al are always totally condensed above the temperature at which MgO reaches 1 wt% of the condensate assemblage, all calculated condensate compositions plotted in these figures have the solar Ca/Al ratio. The paths in Fig. 4a and b differ from those in Grossman et al. (2000) because of the generally finer temperature resolution and updated abundance data employed herein. In particular, because the C/O ratio is 19% greater in this work than in the Anders and Grevesse (1989) abundance table used by Grossman et al. (2000), there is less free oxygen available for oxide and silicate condensates, resulting in slightly lower condensation temperatures in this work, and some changes in condensation sequences.

Discontinuities break each condensation path into segments at temperatures where new phases condense and/or previously condensed phases disappear. Many of the segments in these figures have labels. These are the stable condensate phase assemblages whose bulk compositions are plotted along the segments. It is seen that there are ranges of P^{tot} over which the sequence of condensate assemblages and, consequently, over which the condensation paths are quite similar to one another. Condensation paths may be quite different from one pressure range to another, however. For all $P^{tot} \geqslant 1 \times 10^{-5}$ bar, there is a segment from 7 to 10 wt% MgO and 18 to 20 wt% SiO_2 over which the stable condensates are melilite + spinel + perovskite, the characteristic assemblage of Type A inclusions. The corresponding assemblage at lower P^{tot} is melilite + spinel + Ti-, Al-rich clinopyroxene. As temperature falls, melilite in these assemblages is calculated to react with gaseous Si and Mg to form diopside at $3 \times 10^{-3} \geqslant P^{tot} \geqslant 2 \times 10^{-6}$ bar, creating melilite + spinel + a more Mg-rich clinopyroxene, the characteristic mineral assemblage of Type B CAIs. For $1 \times 10^{-4} \geqslant P^{tot} \geqslant 2 \times 10^{-6}$ bar, this causes the SiO_2 content to rise to >35 wt% where the melilite is exhausted before forsterite condenses. At $P^{tot} \geqslant 1 \times 10^{-3}$ bar, however, forsterite condenses before melilite is exhausted and the condensation path follows a relatively low-SiO_2 trajectory to the right on Fig. 4b. Within this range of P^{tot}, the melilite + spinel + clinopyroxene segment shifts to progressively lower MgO contents with decreasing P^{tot}. No silicate liquids are calculated to be stable at $P^{tot} \leqslant 10^{-1}$ bar for a system of solar composition.

At lower P^{tot}, $<2 \times 10^{-6}$ bar, melilite begins to react to form anorthite before much clinopyroxene forms, and the condensation paths veer toward the upper left on Fig. 4a. A continuous series of condensation paths, corresponding

Table 4
Bulk chemical compositions, corrected to solar CaO/Al_2O_3 and 100 wt% CMAS oxides, and isotopic mass-fractionations of refractory inclusions

Inclusion	TS32	F11 (TS68)	E13	E49A	E49	E55	E56	E62
Meteorite	AL	AL	EF	EF	EF	EF	EF	EF
Type	CTA	CTA	CTA	CTA	CTA	CTA	CTA	CTA
Method	MR	MR	INAA	INAA	MR	INAA	MR	INAA
CaO	30.56	29.91	27.80	29.32	31.00	28.53	31.87	32.99
MgO	10.89	9.68	9.40	12.30	8.99	11.11	7.42	5.73
Al_2O_3	38.60	37.78	35.11	37.03	39.16	36.03	40.25	41.67
SiO_2	19.95	22.64	27.69	21.35	20.85	24.34	20.46	19.60
F_{Mg}	7.63 ± 0.03[c]	4.9 ± 1.3[d]	-1.12 ± 0.03[c]	2.17 ± 0.03	5.41 ± 0.04	1.35 ± 0.13	2.45 ± 0.05[c]	-1.25 ± 0.06
F_{Si}[a]	1.51[c]	1.43[e]	-0.23	1.09	1.48	2.15	1.74	2.99

Inclusion	TS33	TS34	3537-2	F2 (TS65)	F7 (TS67)	1623-8	E107	Golfball	E60
Meteorite	AL	AL	LE	AL	AL	VI[b]	EF	AL	EF
Type	B1	B1	B1	B2	B2	B2	B	B	Fo-B
Method	MR	MR	MR	MR	MR	INAA[g]	MR	MR	INAA
CaO	27.18	27.34	27.60	26.47	25.62	27.51	28.26	24.79	21.07
MgO	10.49	11.79	10.40	11.22	11.86	13.15	11.16	13.32	18.63
Al_2O_3	34.34	34.53	34.86	33.43	32.36	34.72	35.70	31.31	26.61
SiO_2	28.00	26.34	27.14	28.8	30.16	24.62	24.89	30.58	33.69
F_{Mg}	4.18 ± 0.01[c]	5.63 ± 0.14	3.31 ± 0.04[c]	6.12 ± 0.02[c]	4.9 ± 0.6[f]	9.9 ± 0.5[h]	2.07 ± 0.02[c]	1.61 ± 0.03	3.78 ± 0.02[c]
F_{Si}[a]	1.69	1.22[e]	1.56	2.13	1.77[e]	2.73[i]	0.74	0.53	1.74

Uncertainties are $\pm 1\sigma$.
[a] Relative to solar system value.
[b] VI, Vigarano.
[c] Weighted average of values given in Table 2.
[d] Prombo and Lugmair (1986).
[e] Molini-Velsko (1983).
[f] Prombo et al. (1987).
[g] Sylvester et al. (1992).
[h] Loss et al. (1990).
[i] Clayton et al. (1987).

to a relatively narrow interval of P^{tot}, sweeps through the very large region of SiO_2–MgO space that lies between the paths shown for 1×10^{-7} and 1.2×10^{-6} bar. It should be noted that chemical equilibrium requires that the large number of gas–solid reactions implied by the multiple segments between points X and Y along the path for 1×10^{-7} bar in Fig. 4a all occur within a temperature interval of only 12 K. This temperature interval and the number of phase appearances and disappearances shrink as P^{tot} increases from 1×10^{-7} to 1.2×10^{-6} bar. No anorthite stability field was found at 2×10^{-6} bar but, at 1×10^{-5} bar (not shown), anorthite forms more than 50 K below the forsterite condensation temperature, by reaction of spinel with clinopyroxene. This indicates that the much-discussed crossover P^{tot} above which forsterite condenses at a higher temperature than anorthite is $\sim 2 \times 10^{-6}$ bar, rather than $\sim 2.5 \times 10^{-8}$ bar (Petaev and Wood, 1998), $\sim 3.8 \times 10^{-4}$ bar (MacPherson et al., 2004), or $\sim 10^{-5}$ bar (MacPherson et al., 2005). Neither the elemental abundances, nor the thermodynamic data sources nor the nature of the clinopyroxene solution model are given in the latter three papers. Consequently, the relative contributions of these parameters and other factors to the differences among the three literature estimates of the crossover P^{tot}, and between them and the value obtained here are unknown.

4.3. Condensation paths for dust-enriched systems

Fedkin and Grossman (2006) pointed out that the oxidation state of iron in chondrites indicates that much of the material in them formed in systems whose oxygen fugacity, f_{O_2}, was much higher than that expected in a system of solar composition. It has been known since the work of Wood (1967) that one way of enhancing the f_{O_2} of a cosmic gas is by total evaporation of a system which had become enriched in dust relative to gas but is otherwise solar in composition. Ebel and Grossman (2000) showed that not only does the f_{O_2} differ from that of a system of solar composition during condensation in such systems, but so also do condensation sequences and, hence, condensation paths. If CAIs condensed from dust-enriched systems, then their compositions should be compared to condensation paths relevant to such conditions, and those paths may differ from those in Fig. 4a and b. The atomic $Ti^{3+}/(Ti^{3+} + Ti^{4+})$ ratios of fassaite in CAIs are sensitive to f_{O_2}, and range from ~ 0.3 to 0.8, with a mean of ~ 0.54. Grossman et al. (2008) showed that such values indicate that CAIs formed at an f_{O_2} very close to that of a system of solar composition at 1500 K. OC is the anhydrous, C-free chondritic dust component defined by Yoneda and Grossman (1995), in which all Fe in excess of FeS is present as FeO. Enrichment in OC dust relative to gas by

factors of 10 and 100 compared to solar composition results in enhancements in f_{O_2} by factors of 8 and 120, respectively,

at 1500 K. Using $-\ln f_{O_2} \propto 4\ln X_{Ti^{3+}}/X_{Ti^{4+}}$, it can be shown that, if the f_{O_2} of CAI formation were 8 times higher
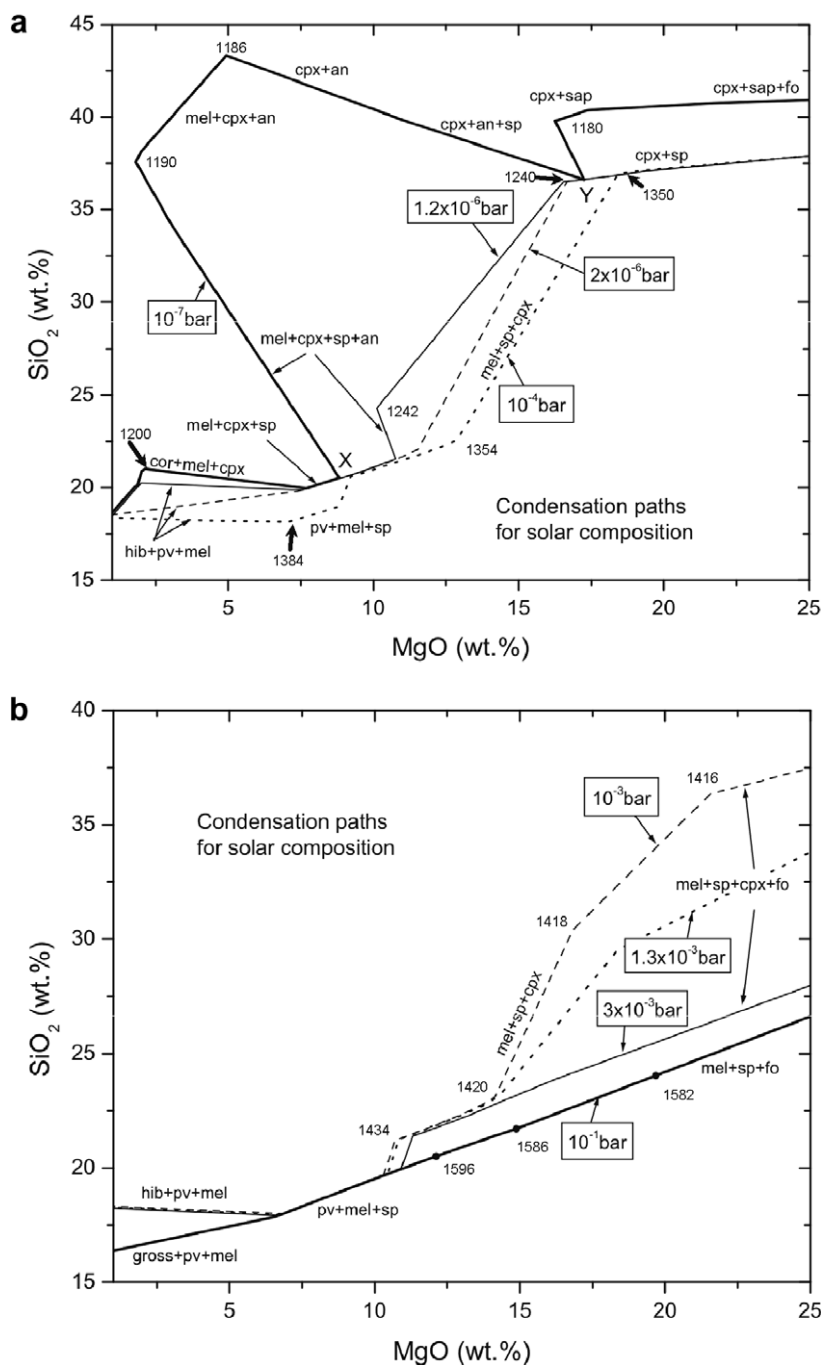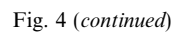

Fig. 4. Condensation paths plotted in SiO_2–MgO space for systems of solar composition at relatively (a) low and (b) high P^{tot}; and for systems enriched in OC dust by a factor of 10 relative to solar composition at relatively (c) low and (d) high P^{tot}. The boxed label on each curve is the P^{tot} assumed for the calculation from which it was obtained. Numbers along paths are temperatures in K. Discontinuities break each path into segments where new phases condense and/or previously condensed phases disappear. Segments are labeled with the stable condensate phase assemblages whose compositions are plotted thereon. In both solar composition and dust-enriched systems, note the relatively broad intervals of P^{tot} over which the characteristic mineral assemblage of Type A inclusions, perovskite + melilite + spinel, and that of Type B inclusions, melilite + spinel + clinopyroxene, are stable, and the relatively small temperature interval over which the former is converted to the latter by reaction of melilite with gaseous Mg and Si to form clinopyroxene, thereby greatly increasing the SiO_2 content of the condensate. *Abbreviations:* cor, corundum (Al_2O_3); hib, hibonite ($CaAl_{12}O_{19}$); gross, grossite ($CaAl_4O_7$); mel, melilite; pv, perovskite; sp, spinel; cpx, clinopyroxene; an, anorthite; fo, forsterite; sap, sapphirine ($Mg_2Al_4SiO_{10}$); liq, CMAS liquid.

Fig. 4 (continued)

than the solar value, the range of $Ti^{3+}/(Ti^{3+} + Ti^{4+})$ ratios in fassaite would be little different from the observed range but, if the f_{O_2} were 120 times higher than the solar value, the range of $Ti^{3+}/(Ti^{3+} + Ti^{4+})$ ratios would be from ~0.1 to 0.5, significantly different from the observed distribution. Accordingly, to model condensation at a dust enrichment plausibly relevant to CAI formation, a set of condensation calculations identical to that described above was carried out for a system enriched in OC dust by a factor of 10.

The resulting condensation paths are shown in Fig. 4c and d. Because the condensation sequences are so similar, the dust-enrichment paths for $10^{-7} \leqslant P^{tot} \leqslant 2 \times 10^{-5}$ bar are very similar to the solar composition paths for $2 \times 10^{-6} \leqslant P^{tot} \leqslant 1 \times 10^{-3}$ bar, and the dust-enrichment paths for $5 \times 10^{-5} \leqslant P^{tot} \leqslant 1 \times 10^{-3}$ bar are very similar to the solar composition paths for $3 \times 10^{-3} \leqslant P^{tot} \leqslant 1 \times 10^{-1}$ bar. Furthermore, as in solar composition, forsterite condensation prior to much clinopyroxene formation leads to a family of condensation paths extending to

high-MgO contents at intermediate SiO_2 contents over a narrow range of P^{tot}, between 2×10^{-5} and 5×10^{-5} bar in this case. For $4 \times 10^{-3} \leqslant P^{tot} \leqslant 1 \times 10^{-1}$ bar, however, the dust-enrichment paths are distinct from any of the solar composition paths seen in Fig. 4a and b. This is due to the stability of CMAS liquids at these pressures for the dust enrichment considered here. Within this range of P^{tot}, the liquid stability field increases in size with increasing P^{tot}. On the path for 1×10^{-2} bar, liquid forms along the near-vertical segment at ∼10 wt% MgO, and results from the reaction of melilite with the gas to form a CMAS condensate liquid with falling temperature. That path continues as a straight line proceeding toward the upper right with falling temperature, along which spinel + liquid ± perovskite is the stable phase assemblage before being joined by forsterite. At 10^{-1} bar, in contrast, CMAS liquid + spinel ± perovskite is the stable phase assemblage even for MgO contents below 10 wt%, replacing the high-temperature melilite stability field found at 1×10^{-2} bar. At intermediate P^{tot}, 1.1×10^{-2} bar, the stability field of CMAS liquid + spinel ± perovskite is split, with melilite crystallizing from the liquid with falling temperature and then reacting with the gas at still lower temperature to form CMAS liquid again. Because the melilite–liquid phase relations are very poorly predicted by the CMAS liquid model employed here (Grossman et al., 2002), the paths shown at the extreme left of Fig. 4c and d should be considered quite uncertain. This is of little consequence to the conclusions of this work.

4.4. Bulk compositions of CAIs compared to condensation paths

For each inclusion, a point corresponding to the SiO_2 and MgO contents given in Table 4 is plotted as a bold symbol in each of Fig. 5a and b, filled for Type A inclusions and open for Type Bs. Condensation paths for solar composition are shown for reference, at relatively low values of P^{tot} in Fig. 5a and relatively high P^{tot} in Fig. 5b. The plain symbols that surround the bold symbol of the same shape correspond to the compositions generated by the possible variations in mineral proportions that were averaged to yield the composition indicated by the bold symbol. In each of Fig. 5a and b, each inclusion thus plots as a field, circumscribed by a solid curve if it is a Type A and a dotted curve if a Type B, within which lies the actual composition. The reason why these fields are not described by the usual orthogonal error bars is that they do not arise from uncertainty in measurements of independent parameters but rather from correction for assumed over- or under-sampling of stoichiometric phases with specific Mg/Si ratios.

Inspection of Fig. 5a and b reveals that Type B inclusions have higher average SiO_2 and MgO contents, 27.6 ± 2.1 and 11.7 ± 1.0 wt%, respectively, than Type As, 22.1 ± 2.6 and 9.4 ± 2.0 wt%. This comparison excludes E60, whose forsterite-rich composition makes it atypical of Type B inclusions. Furthermore, while almost all Type Bs have higher SiO_2 contents than almost all Type As, there is more overlap in the MgO contents of the two inclusion types. The classification of inclusion E107 is problematic. While it contains only ∼20 vol % fassaite, which would make it a Type A, it also contains a few grains of primary anorthite, which would make it a Type B. Furthermore, its fassaite contains an average of ∼9 wt% total Ti oxides, which is less than the minimum level seen in fassaite in CTAs, ∼15 wt% (Simon et al., 1999). E107 is thus classified a Type B in this work. Appropriately, in Fig. 5a and b, its bulk composition plots in the border region between the Type A and Type B fields.

Inspection of Fig. 5a and b shows that the observed compositions of six of the eight Type A inclusions lie within error of the calculated condensation path for 1.2×10^{-6} bar, while that of E49A is compatible with the path for 3×10^{-3} bar and that for E13 would lie on one of the family of paths lying between 1.2×10^{-6} and 1×10^{-7} bar. In contrast, five of the nine Type Bs would lie within that family of paths, three others on the curves that would lie between those for 1.2×10^{-6} and 1×10^{-4} bar, and the final one, E60, on a path near that for 1×10^{-3} bar. Compared to the condensation paths for $1 \times 10^{-4} \leqslant P^{tot} \leqslant 1 \times 10^{-1}$ bar, the observed compositions of all Type B inclusions are too low in MgO for their SiO_2 contents, just as was noted by Grossman et al. (2000).

The same data plotted in Fig. 5a and b are plotted in Fig. 6a and b, where they are compared to condensation paths for systems enriched in OC dust by a factor of 10. The dust-enrichment path for 10^{-7} bar passes through the fields of five of the eight Type A inclusions and very close to that for a sixth, E55, while the compositions of E13 and E49A require $P^{tot} \geqslant 10^{-2}$ and ∼10^{-4} bar, respectively. While the compositions of three of the nine Type B CAIs lie along the path for 10^{-2} bar and that of TS33 lies very close to it, those of E107 and TS34 lie close to a curve in the vicinity of 4-6 × 10^{-3} bar, that of E60 lies on the path for 2×10^{-5} bar, and that of 1623-8 lies close to a curve in the vicinity of 1×10^{-6} bar. No dust-enrichment path has been found that is compatible with the composition of F7.

Grossman et al. (2000) assumed that the heavy-isotope enrichments of Mg and Si in CAIs are the result of partial evaporation of these elements after the inclusions condensed, and argued that the present-day compositions of the inclusions, such as those plotted in Figs. 5 and 6, were modified in that evaporation event. In the following sections, the Mg- and Si-isotopic compositions are used to estimate the bulk chemical compositions of the inclusions prior to evaporation in order to see if their unmodified compositions agree with predictions of condensation models.

4.5. Fractions of Mg and Si evaporated

Due to the possible presence of excess ^{26}Mg from decay of extinct ^{26}Al in these samples, determination of F_{Mg}, the Mg mass-fractionation, is based on the $\delta^{25}Mg$ data. For each inclusion for which multiple measurements of $\delta^{25}Mg$ were made, a mean value was obtained by weighting the individual measurements on Table 2 by the inverse square of their uncertainties. These data are shown in Table 4, along with literature values for three other inclusions, F11, F7 and 1623-8. Because the terrestrial Mg
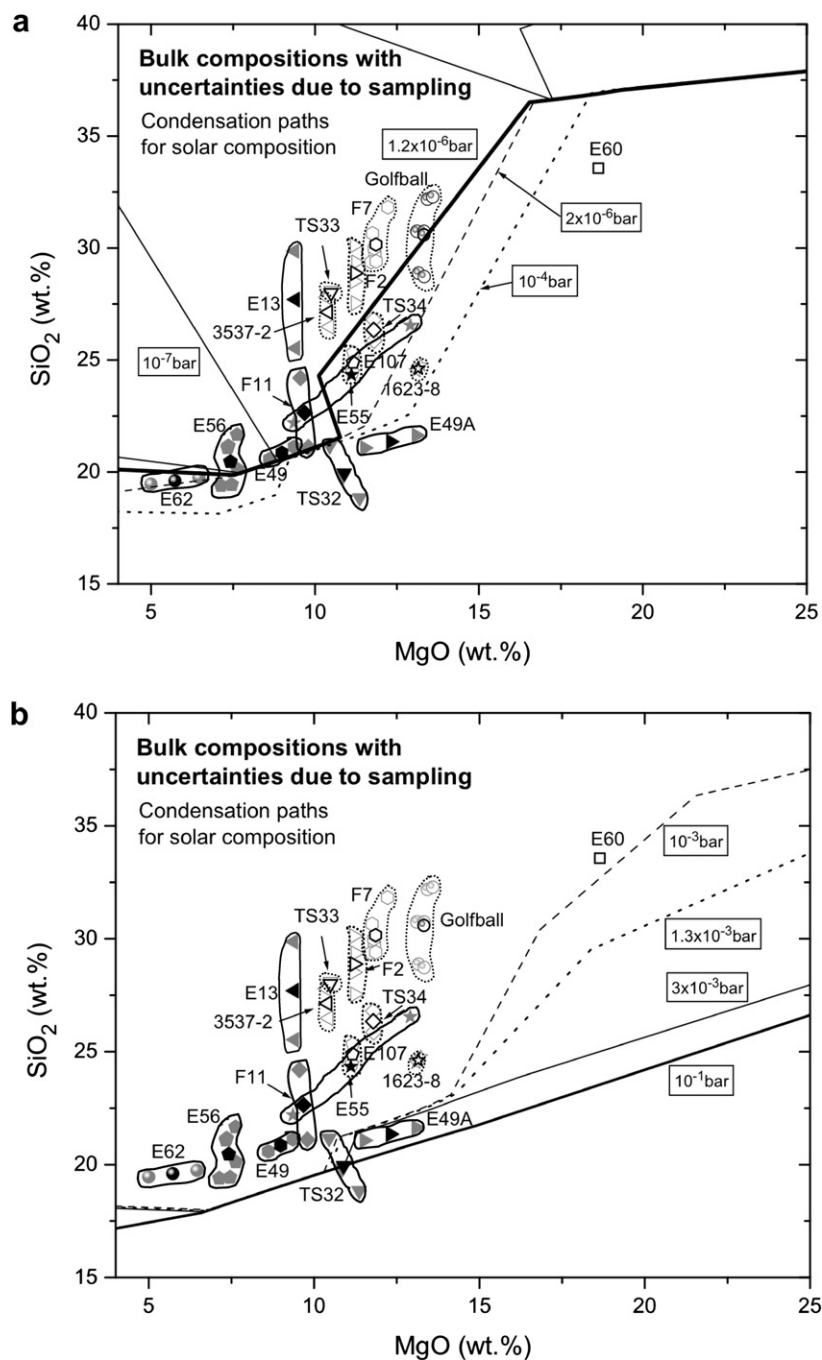
Fig. 5. Best estimates of the present-day bulk SiO_2 and MgO contents (bold symbols) of all inclusions in this study, and their possible variations (plain symbols) due to non-representative sampling in the laboratory. Filled symbols with fields circumscribed by solid curves—Type A inclusions; open symbols with fields circumscribed by dotted curves—Type Bs. SiO_2 contents of most Type Bs are higher than those of most Type As, while there is more overlap in MgO contents. Condensation paths calculated for a system of solar composition at relatively (a) low P^{tot} and (b) high P^{tot} are shown for reference. Observed compositions of six of eight Type A inclusions are within error of the path for $P^{tot} = 1.2 \times 10^{-6}$ bar (bold). Compared to all paths for $P^{tot} \geqslant 10^{-4}$ bar, observed compositions of all Type B inclusions are too low in MgO for their SiO_2 contents.

standard employed in this work has the same isotopic composition as Orgueil (Galy et al., 2003), it is assumed that the F_{Mg} data for the inclusions are relative to the mean Mg-isotopic composition of condensed solar system matter.

For each inclusion, the mean $\delta^{30}Si$ on Table 2 was divided by 2 to obtain F_{Si}, the Si mass-fractionation. Molini-Velsko et al. (1986) found that bulk meteorites have $\delta^{30}Si$ of $-0.55\permil$ relative to NBS-28, indistinguishable from the value of $-0.58 \pm 0.06\permil$ found by Georg et al. (2007), so
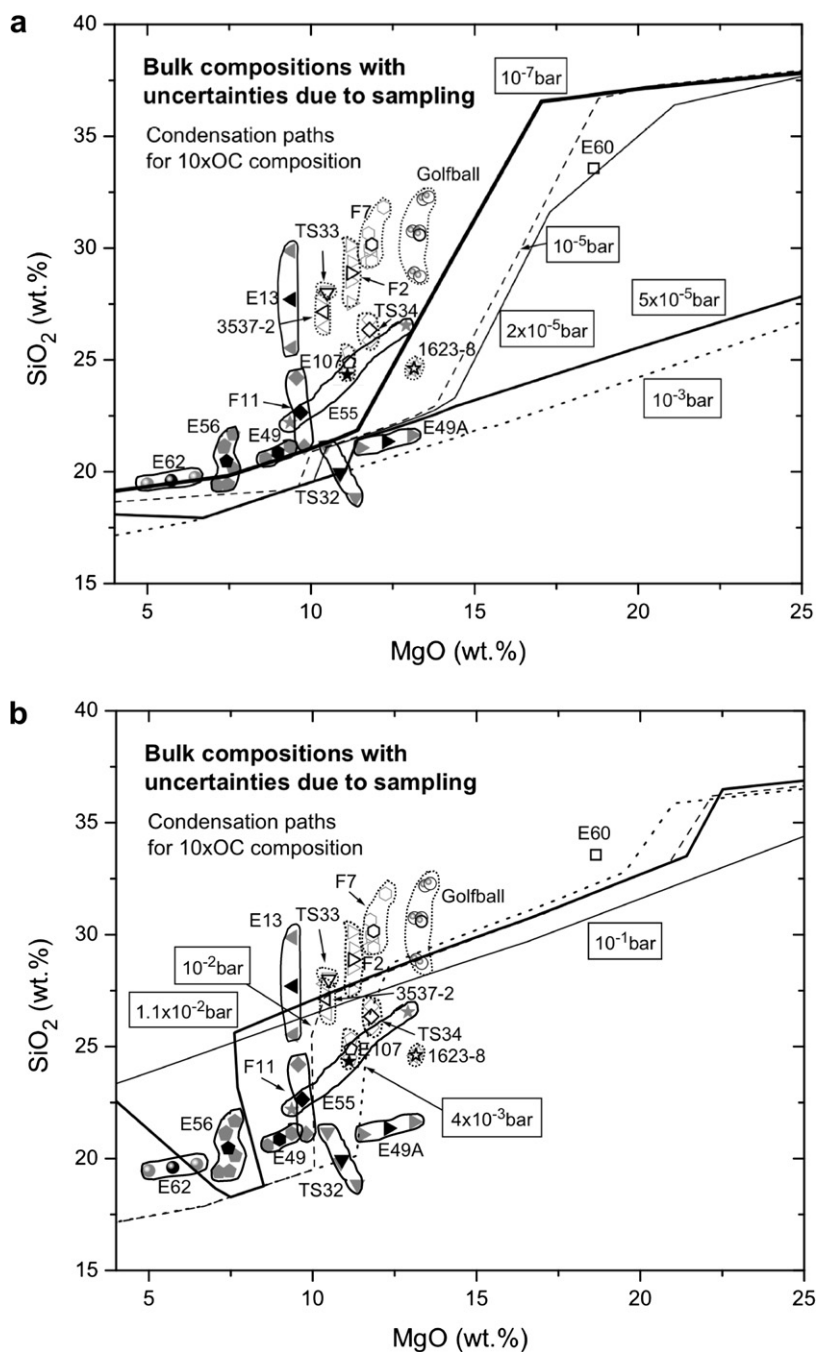
Fig. 6. The same data points as in Fig. 5 compared to condensation paths calculated for a system enriched by a factor of 10 in OC dust relative to gas compared to solar composition at relatively (a) low P^{tot} and (b) high P^{tot}. While the compositions of many Type A inclusions are compatible with the path for $P^{tot} = 10^{-7}$ bar (bold), Type Bs do not concentrate along any particular path. Symbols as in Fig. 5.

the former was assumed to represent average solar system matter and the isotopic composition of CAIs when they condensed. Since all silicon-isotopic data on Table 2 and those taken from the literature for TS34, F11, F7 and 1623-8 were measured relative to NBS-28, all the F_{Si} data used in this work were increased by 0.275‰ in order to express their deviation from mean solar system matter. These are the data given in Table 4.

For those samples whose isotopic compositions were measured in this work, the F_{Si} and F_{Mg} data on Table 4 are plotted against one another in Fig. 7a for Type A inclusions and in Fig. 7b for Type Bs. All of the data from the study of Grossman et al. (2000) are also plotted on Fig. 7a and b, and these include the literature data for F11, F7 and 1623-8 that also appear on Table 4. Among the four Type A inclusions whose isotopic data were sum-

Fig. 7. Isotopic mass-fractionation of Si, F_{Si}, plotted against that of Mg, F_{Mg}, both relative to mean solar system matter, of all (a) Type A and (b) Type B inclusions in this study. Data compiled by Grossman et al. (2000) are shown for reference. Error bars are 1σ.

study, the major difference being that the most fractionated inclusion in the present work has F_{Si} and F_{Mg} of 2.1 and 6.1‰/amu, respectively, much less than the most fractionated inclusions in the earlier work whose F_{Si} and F_{Mg} are 3.8 and 9.0‰/amu (3675A) and 2.7 and 9.9‰/amu (1623-8), respectively. None of the Type Bs in either study has negative F_{Si} or F_{Mg}.

If, as in Grossman et al. (2000), it is assumed that the heavy-isotope enrichments in Mg and Si result from kinetic isotope fractionation that occurred during evaporation into a low-density gas while the inclusions were molten, the fraction of each element remaining, f_{rem}, can be calculated using the Rayleigh equation,

$$R/R_o = f_{rem}^{\alpha-1}, \tag{1}$$

where α is the isotopic fractionation factor for evaporation of the element in question from this specific matrix, R is the observed isotope ratio of the element and R_o is the initial isotope ratio, here taken as the mean isotopic composition of the element in condensed solar system matter.

Isotopic fractionation factors have been determined for Mg and Si by measuring the isotopic compositions of residues produced by evaporation of CMAS liquid compositions similar to those of Type B inclusions in vacuum and hydrogen as a function of temperature. Knight et al. (2007) found that $(1-\alpha)$ for Si evaporation is 0.0103 ± 0.0007, independent of temperature. Richter et al. (2005) found that $(1-\alpha)$ for Mg evaporation is a linear function of inverse temperature. Using petrologic constraints, Grossman et al. (2002) suggested that the average temperature for evaporation of Type A CAI liquid compositions is ~1775 K and that for Type Bs is ~1675 K. At 1775 K, $(1-\alpha)$ for Mg is 0.01203 ± 0.00073 and, at 1675 K, the extrapolated value is 0.011.

For each inclusion in Table 4, the fraction of each of the Mg and Si evaporated was calculated from the isotopic composition for each element and the element's fractionation factor at the appropriate temperature for each inclusion type. Excluded from this calculation are the Type A inclusions E13 and E62, because of their negative F_{Si} and/ or F_{Mg}. The significance of these light-isotope enrichments will be discussed later. Results for the remaining inclusions are plotted in Fig. 8. There appears to be little difference in the degree of evaporation of these elements between Types A and B inclusions.

4.6. Initial chemical compositions of CAIs

For each inclusion plotted in Fig. 8, the amounts of MgO and SiO₂ evaporated were added back to the present-day bulk chemical composition in Table 4 to obtain the initial bulk chemical composition by renormalization to 100 wt %. The results, listed in Table 5, are the compositions that each CAI had before evaporation caused Mg and Si loss, referred to herein as the pre-evaporation compositions. The pre-evaporation SiO₂ and MgO contents are plotted in Fig. 9a and b, where they are compared to condensation paths for solar composition, and in Fig. 10a and b, where they are compared to condensation paths for 10 × OC dust enrichment. For each inclusion, every

marized by Grossman et al. (2000), three have positive F_{Si}, between 1 and 2.6‰/amu, and positive F_{Mg}, between 5 and 11‰/amu. One has negative F_{Si} with relatively low F_{Mg} of ~2‰/amu. Among the seven Type As analyzed in this work, five have both positive F_{Si} and positive F_{Mg}. The F_{Si} values fall in a relatively narrow range between 1 and 2.2‰/amu, while their F_{Mg}s range between 1 and 8‰/amu. The other two Type As studied here, E13 and E62, have negative F_{Mg}, and one of the latter, E13, also has negative F_{Si}. Among the Type Bs considered by Grossman et al. (2000), F_{Si} is positively correlated with F_{Mg}, and this is also the case for the Type Bs analyzed in the present
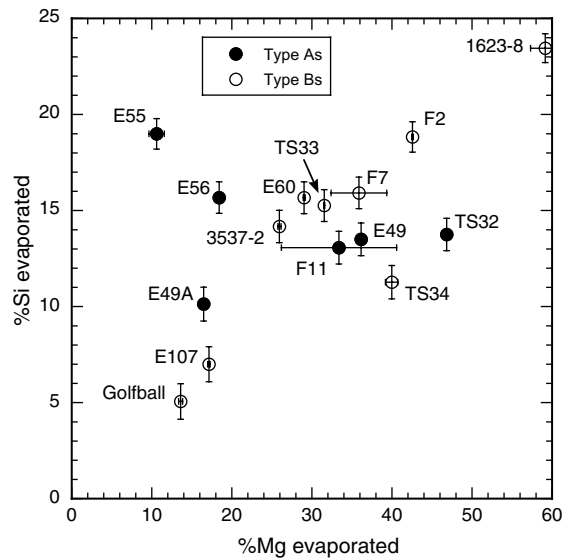
Fig. 8. Fractions of Mg and Si evaporated for all inclusions in this work whose F_{Mg} and F_{Si} are both positive. Filled symbols are for Type A inclusions and open symbols are for Type Bs.

member of the cluster of points representing the possible range of present-day compositions in Figs. 5 and 6, is itself transformed into a new cluster of points in Figs. 9 and 10 due to propagation of the uncertainty in Mg- and Si-isotopic compositions. For clarity, the latter uncertainty is not propagated for the mean composition of each inclusion, which is again plotted as a bold symbol. For each inclusion, the pre-evaporation composition lies within the field that circumscribes the plain symbols for that inclusion. Inspection of Figs. 9 and 10 reveals that the pre-evaporation compositions of Type Bs are even more clearly separated from those of Type As than are the observed compositions, corrected for non-representative sampling, in Figs. 5 and 6. While there is still considerable overlap in MgO content be-

tween the two inclusion types, the average pre-evaporation SiO_2 content of Type Bs, excluding the forsterite-bearing one, E60, is 28.9 ± 2.6 wt%, while that of Type As is only 23.4 ± 2.6 wt%. Inclusion E107 again has a composition falling between most Type A and most Type B inclusions.

In comparing chemical compositions of CAIs with condensation paths for solar composition, it is clear that the pre-evaporation compositions in Fig. 9a and b are shifted toward condensation paths for higher P^{tot} compared to their present-day compositions in Fig. 5a and b, respectively. It is also clear that no single condensation path can pass through all inclusion compositions. The composition fields of a remarkably large fraction of the inclusions, however, four of six Type As and six of nine Type Bs, are intersected by a subset of the condensation paths calculated for a relatively narrow range of P^{tot}, between 1.2×10^{-6} and 1×10^{-4} bar. The Type A exceptions are E56, which would seem to require P^{tot} below 1.2×10^{-6} bar, and TS32, requiring P^{tot} slightly greater than 10^{-1} bar. The Type B exceptions are TS34 and 1623-8, requiring P^{tot} of $\sim 2 \times 10^{-3}$ bar and slightly greater than 10^{-1} bar, respectively, and the forsterite-bearing inclusion, E60, requiring P^{tot} of $\sim 10^{-3}$ bar. Recall, however, that 1623-8 and E60 are two of the CAIs whose compositions were determined by INAA, so it is conceivable that their actual compositions lie slightly outside their fields on Fig. 9. Similarly, when pre-evaporation compositions are compared with condensation paths for enrichment in OC dust by a factor of 10 in Fig. 10a and b, it is again clear that no single path can account for all inclusion compositions. The path for $P^{tot} = 1.1 \times 10^{-2}$ bar (Fig. 10b) passes through the fields of five of the nine Type Bs and one of the six Type As, and comes very close to that for another Type A, E56. Another path, at $P^{tot} = 3 \times 10^{-5}$ bar, would pass through the fields of three of the remaining Type As, one of the remaining Type Bs and E60. This leaves only three inclusions unaccounted for. E107 and 1623-8, Type Bs, require P^{tot} near 1×10^{-7} and slightly greater than 1×10^{-3} bar,

Table 5
Original, pre-evaporation chemical compositions of refractory inclusions, calculated from the compositions and isotopic mass-fractionations given in Table 4

Inclusion	TS32	F11 (TS68)	E49A	E49	E55	E56	TS33	TS34
Meteorite	AL	AL	EF	EF	EF	EF	AL	AL
Type	CTA	CTA	CTA	CTA	CTA	CTA	B1	B1
CaO	27.10	27.63	27.97	28.61	26.66	30.22	24.73	24.59
MgO	18.16	13.42	14.05	12.99	11.61	8.62	13.95	17.66
Al_2O_3	34.23	34.90	35.32	36.15	33.66	38.16	31.25	31.05
SiO_2	20.51	24.06	22.66	22.25	28.07	23.00	30.07	26.70

Inclusion	3537-2	F2 (TS65)	F7 (TS67)	1623-8	E107	Golfball	E60
Meteorite	LE	AL	AL	VI	EF	AL	EF
Type	B1	B2	B2	B2	B	B	Fo-B
CaO	25.53	23.01	22.80	21.73	27.12	23.90	18.50
MgO	12.99	16.99	16.46	25.44	12.93	14.86	23.05
Al_2O_3	32.24	29.07	28.80	27.43	34.26	30.18	23.37
SiO_2	29.24	30.93	31.93	25.41	25.69	31.06	35.08

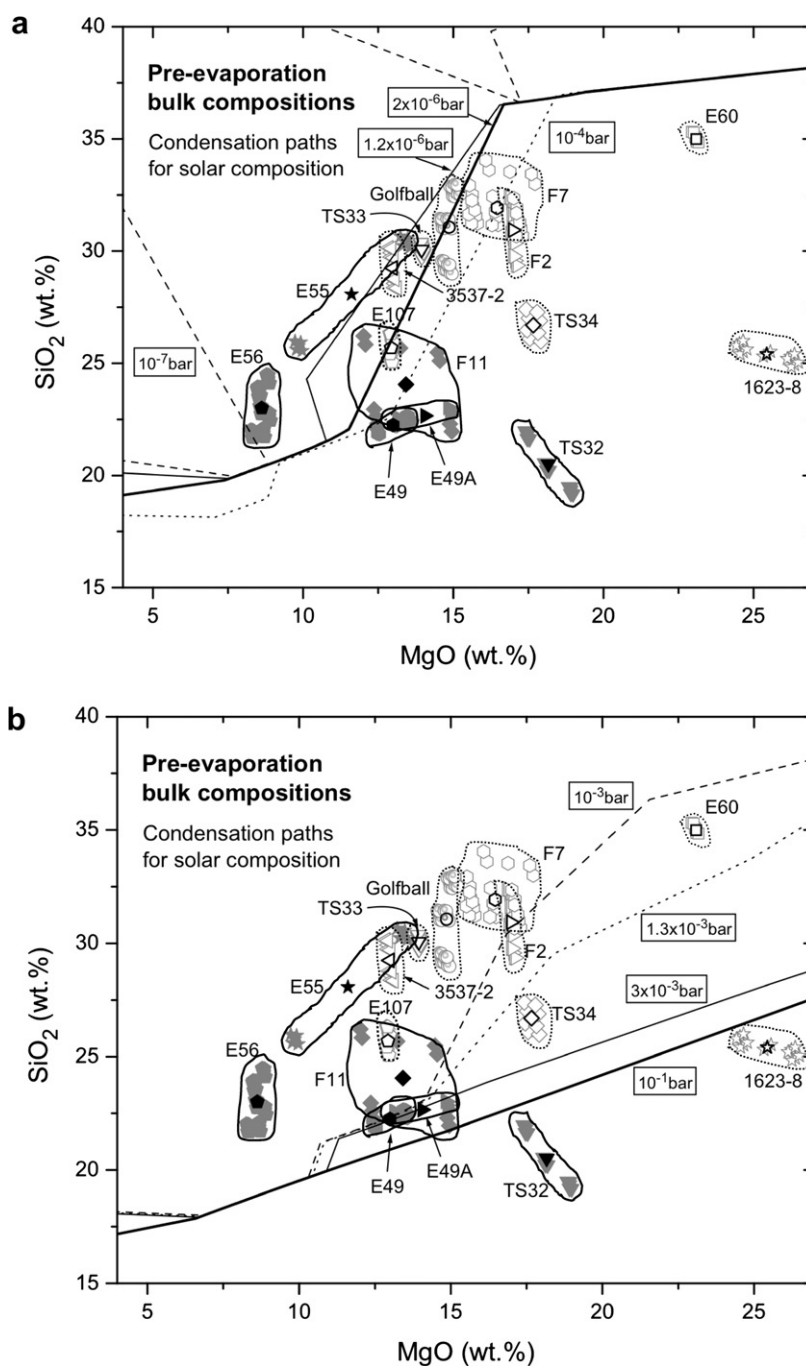Meteorite name abbreviations as used previously.

Fig. 9. Initial, pre-evaporation bulk chemical compositions of the inclusions of this study, compared to condensation paths for systems of solar composition at relatively (a) low P^{tot} and (b) high P^{tot}. Prior to evaporation, most Type B inclusions had higher SiO$_2$ contents than most Type As. Compositions of many inclusions are compatible with those of equilibrium condensate assemblages formed at P^{tot} between 1.2×10^{-6} and 1×10^{-4} bar, represented by the path for $P^{tot} = 2 \times 10^{-6}$ bar (bold) in (a). Symbols as in Fig. 5.

respectively. TS32, a Type A, also requires P^{tot} slightly higher than 1×10^{-3} bar.

In summary, compatibility of most pre-evaporation compositions with condensation paths for dust enrichment tends to occur at higher values of P^{tot} than with those for solar composition. Regardless of which set of condensation paths is used for comparison, the variation in pre-evaporation compositions requires that the population of inclusions

studied here originated in nebular zones of widely different P^{tot}. Ruden and Pollack (1991) calculated the variation of the midplane temperature and pressure with time and distance from the center of the solar nebula for three different disk masses between 0.11 and 0.38 solar masses, and a turbulence parameter, $\alpha = 10^{-2}$. In the high-mass case, for example, the midplane cools from ~1600 to 1400 K while the midplane pressure falls from 3×10^{-4} to 1×10^{-4} bar
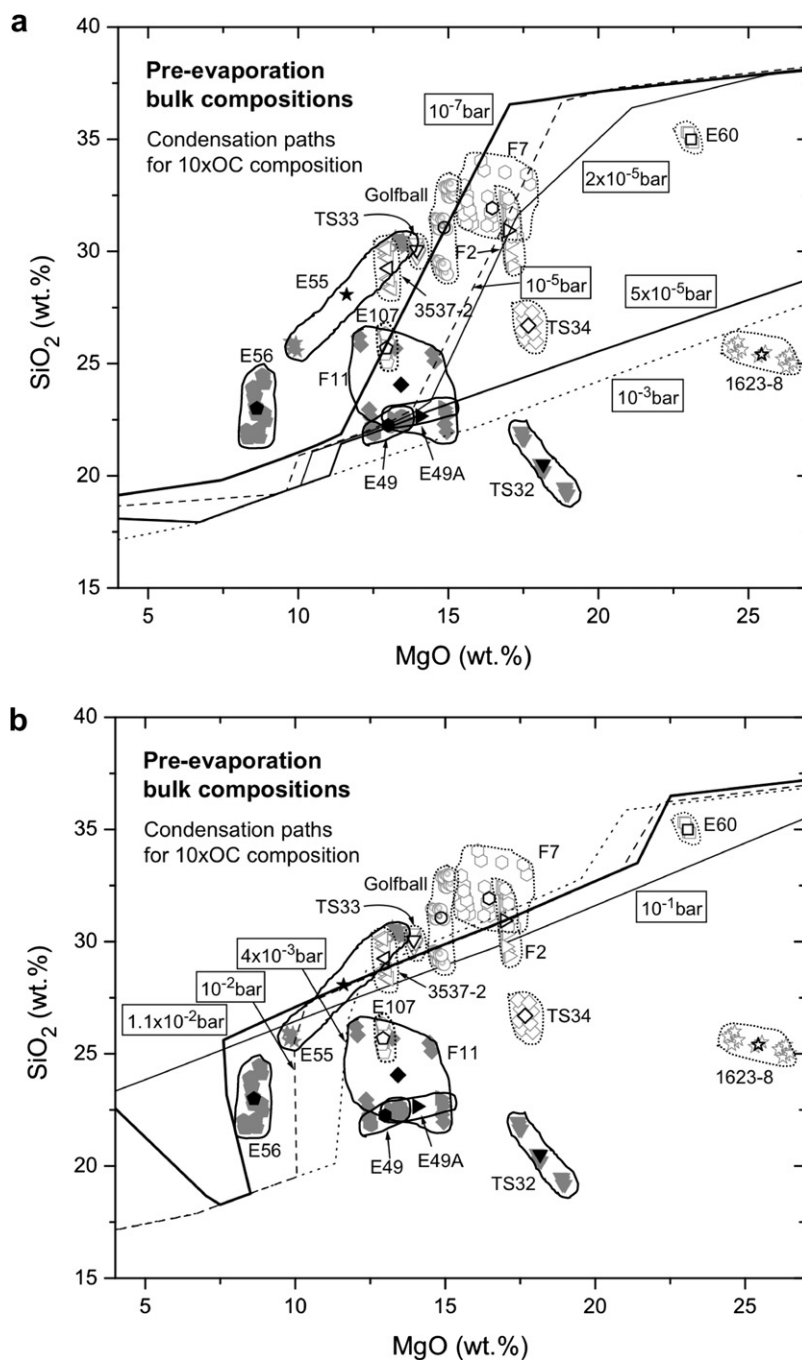
Fig. 10. Initial, pre-evaporation bulk chemical compositions of the inclusions of this study, compared to condensation paths for a system enriched by a factor of 10 in OC dust relative to gas compared to solar composition at relatively (a) low P^{tot} and (b) high P^{tot}. The compositions of six inclusions are compatible with condensation at $P^{tot} = 1.1 \times 10^{-2}$ bar (bold). Symbols as in Fig. 5.

in 2.2×10^4 year at 1 a.u., and from ~1400 to 1100 K while the pressure falls from 4×10^{-5} to 1×10^{-5} bar at 2 a.u. In all cases considered, wherever and whenever the temperature is within the range of silicate condensation temperatures, 2000–1000 K, P^{tot} lies between 6×10^{-6} and 6×10^{-3} bar, a range little different from that with which most of the above inclusions are compatible.

Much of the variation in P^{tot} inferred from Figs. 9 and 10 is due to a relatively wide range of MgO in the pre-evap-

oration compositions. In both figures, a significant number of inclusions plot within a family of condensation paths, representing a range in P^{tot}, along which a sharp rise in SiO$_2$ content occurs from ~21 to 36 wt%. The increase in SiO$_2$ content is due to reaction of åkermanitic melilite with the gas to form diopsidic clinopyroxene. With increasing P^{tot}, this increase occurs at higher MgO content, due to higher åkermanite content of melilite, beginning at ~11 wt% at 2×10^{-6} bar on Fig. 9a and ~14 wt% at

1.3×10^{-3} bar on Fig. 9b, for example. If the increase in the åkermanite content of melilite, a diffusion-controlled process, had failed to keep up with falling temperature at any particular P^{tot}, clinopyroxene condensation might have begun when the bulk assemblage had a lower MgO content than predicted by the model. A wide range of bulk MgO contents could conceivably result from condensation at fixed P^{tot} if different inclusions were affected differentially by this departure from equilibrium.

Pre-evaporation compositions are expected to fall along calculated condensation paths only if each inclusion is a representative sample of the non-metallic condensates that existed at a given temperature in a system of the assumed composition and pressure. At temperatures below that where melilite reacts to form clinopyroxene, forsteritic olivine is the next major condensate mineral to form along most condensation paths shown in Figs. 9 and 10. Forsterite differs from spinel, melilite and clinopyroxene in that its condensation does not involve reaction of pre-existing solid phases with the gas. Thus, all of the major components of forsterite condense directly from the gas. In order for a preexisting nodule of spinel + clinopyroxene to remain on a given condensation path after forsterite formation, the nodule must mix with independently condensed forsterite in the exact proportions in which they occur in the nebula. Because the condensate forsterite plots at ~43 wt% SiO_2 and ~56 wt% MgO, addition of slightly more or less than the equilibrium proportions of this phase at a given P^{tot} could broaden the distribution of pre-evaporation compositions in Figs. 9 and 10 mostly in the MgO direction, making them appear to represent condensates from a wide range of P^{tot}.

If the present-day bulk chemical compositions of CAIs were exactly as measured, corrections for non-representative sampling in the laboratory would not be justified. Although cogent reasons for believing that sampling bias is indeed a problem were given by Simon and Grossman (2004), the above exercise of determining the pre-evaporation compositions of CAIs could have been based on their raw, bulk chemical compositions rather than on their compositions corrected for non-representative sampling. Such an exercise would have yielded no information about P^{tot} or dust/gas ratio during condensation, however, as all calculated condensate assemblages whose compositions contain significant MgO (Fig. 4) have solar Ca/Al ratios. Indeed, a possible interpretation of the raw, present-day, non-solar Ca/Al ratios of CAIs is that their bulk chemical compositions bear no relationship to specific condensation paths, and arriving at this interpretation does not require determination of pre-evaporation compositions. The present work is predicated on the assumption that each CAI is a representative sample of the equilibrium condensate assemblage formed at a specific temperature, P^{tot} and system composition.

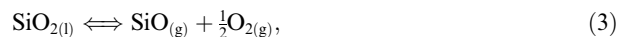## 4.7. Forward kinetic modeling of evaporative change in composition

In this work, the original chemical compositions of CAIs were calculated from their observed compositions using isotopic data only, under the assumption that the heavy-isotope enrichments of Mg and Si are the result of evaporation of partially molten CAIs. As a test of this assumption, forward kinetic modeling was performed to see if each observed chemical composition could be regenerated from its corresponding pre-evaporation composition using only thermodynamic and kinetic data for CMAS liquids, completely independent of the isotopic data. In performing this exercise, it is not sufficient merely to regenerate any composition within the field for a CAI in Fig. 5 from a starting point that lies anywhere within its respective field in Fig. 9. This is because the isotopic compositions were used to translate each point that defines the field for a given CAI in Fig. 5, into a corresponding point in Fig. 9 that was broadened into a cluster of points by propagating the uncertainty in the isotopic compositions. The area of that cluster of points is only a fraction of the area occupied by the field for a given CAI in Fig. 9. The exercise can only be considered a success if any point within one of those small clusters of points in Fig. 9 can be used to regenerate its point of origin in Fig. 5.

Kinetic modeling of the change in composition with progressive evaporation was performed as in Grossman and Fedkin (2003) but with some significant differences. A droplet radius of 0.25 cm, an ambient P_H^{tot} of 1×10^{-3} bar, and a closed system of solar composition were assumed. Use of different values for the droplet radius and ambient P_H^{tot} would change the rate at which the chemical composition of the droplet evolves but not its path in MgO–SiO$_2$ space. The assumption that the Ca/Al ratio is solar in each pre-evaporation composition implies that 100% of the Al and Ca were condensed into the droplet. The initial distributions of Mg and Si between droplet and gas were calculated by comparing the Mg/Al and Si/Al ratios of the pre-evaporation composition to their respective solar ratios. In addition to these four elements, the system was assumed to contain H, He, C, N, O, P and S in solar proportions. At each evaporation step, gas-phase equilibrium was used to compute the partial pressures, P_i^a, of all significant species i in the ambient gas, uninfluenced by the droplet. The vapor pressures, P_i^v, of $Mg_{(g)}$ and $SiO_{(g)}$ were calculated at each step from the equilibria,

$$MgO_{(l)} \Longleftrightarrow Mg_{(g)} + \tfrac{1}{2}O_{2(g)} \tag{2}$$

and

$$SiO_{2(l)} \Longleftrightarrow SiO_{(g)} + \tfrac{1}{2}O_{2(g)}, \tag{3}$$

using the Berman (1983) relationship between component activities and composition in CMAS liquids, and the f_{O_2} of the ambient gas. This is equivalent to assuming that the droplet and ambient gas were in redox equilibrium during evaporation, an assumption that is justified by the fact that the oxidation state of Ti in real CAIs is that expected from equilibrium in a system of solar composition. The flux of each species, J_i, is calculated from the Hertz–Knudsen equation which, for $Mg_{(g)}$, for example, is written

$$J_{Mg} = \frac{\alpha_{Mg}\left(P_{Mg}^v - P_{Mg}^a\right)}{\sqrt{2\pi MRT}}, \tag{4}$$

where α_{Mg}, M, R and T are the evaporation coefficients and molecular weight of $Mg_{(v)}$, the gas constant and temperature, respectively. Data for α_{Mg} and its temperature dependence were taken from evaporation experiments on CMAS liquids by Richter et al. (2002), and α_{SiO} was assumed to be $\alpha_{Mg} \times 1.425$, as found at 1500 K in H_2 in the same work. The composition change in each evaporation step was obtained by multiplying the flux of each species by the time-step size and the surface area of the droplet, the latter reduced by the computed equilibrium volume proportions of crystalline spinel and melilite.

The strategy was to use the pre-evaporation composition as the starting material, and to calculate the change in its composition due to isothermal evaporation in order to see how close the evolutionary path comes to the specific observed composition from which the pre-evaporation composition was inferred. Various pairs of pre-evaporation and observed compositions were attempted for each inclusion. Because experimental petrologic evidence reviewed by Grossman et al. (2002) suggests that peak temperatures experienced by compact Type As and Type Bs were ~1773 and 1673 K, respectively, evaporation temperatures selected for modeling were usually within ±50 K of these values.

Shown in Fig. 11 for each inclusion is the pair of pre-evaporation and observed compositions for which the com-

puted evaporation curve comes closest to the observed composition. For the assumptions stated above, results are very good to excellent for four of six Type A inclusions. Results for the remaining two Type As, E49A and E55, are very poor. The rate of evaporation of Mg relative to that of Si increases with the Mg/Si ratio of the starting material, and this effect is clearly seen in comparing the slopes of the model curves for E49 and E55, which were computed at the same temperature. Although the pre-evaporation compositions of E49A and E49 selected for Fig. 11 are almost identical, their corresponding observed compositions are quite different, implying that their thermal histories are different. Thus, while the observed composition of E49 is intersected perfectly by the isothermal evaporation curve for 1723 K, the lower limit temperature used for modeling Type As, the observed composition of E49A is poorly fit even when the model temperature is 50 K lower, as illustrated by the dashed curve in Fig. 11. For E55, there is no temperature for which an evaporation curve can be found that joins the pre-evaporation and observed compositions.

Failure of this exercise to reproduce the observed chemical composition of an evaporation residue from that of its calculated precursor indicates that the initial and final compositions are not related by a simple, one-stage Rayleigh distillation process. One reason for this may be the conditions of evaporation. Elevation of the partial pressures of the evaporating elements in the ambient gas may have caused the relative evaporation rates of $Mg_{(g)}$ and $SiO_{(g)}$ to differ from those calculated here. If evaporation rates were large compared to diffusion rates of the evaporating elements through the liquid, gradients in the SiO_2/MgO ratio could have developed, causing the relative vapor pressures and thus the relative evaporation rates to differ from those of a homogeneous liquid, which is assumed in the present calculation. The evaporation temperatures employed here are based on inclusion textures that formed when these objects last crystallized from their host liquids. If, however, an inclusion underwent multiple evaporation and crystallization cycles, there is no constraint on the evaporation temperatures during any but the last such cycle. In this case, better agreement with the observed chemical composition of a particular evaporation residue could be achieved by recalculating its path in Fig. 11 in segments, each for a different evaporation event with its own temperature. Finally, if the starting material incorporated either isotopically normal material that failed to equilibrate its isotopic composition with the evaporating liquid or isotopically anomalous relics, prediction of the chemical composition of the starting material from the observed bulk isotopic composition would yield a spurious result. Another reason for the departure of the calculated chemical composition of a residue from the observed one could be due to analytical error. In this regard, it is worth noting that E49A and E55 are the only Type As plotted whose observed compositions were determined by INAA, so the uncertainties on their compositions may be greater than estimated, for the reasons stated above.

Results for Type Bs are excellent except for E60, for which the curve misses by 1% SiO_2. There are two possible reasons why the modeling result for this inclusion is poorer
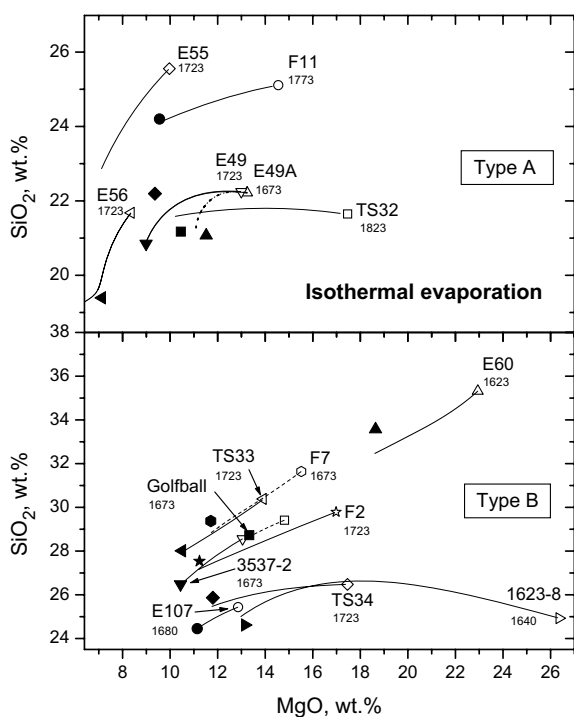

Fig. 11. Computed curves tracing evaporative losses of MgO and SiO_2 for pairs of pre-evaporation and observed compositions for which computed curves come closest to the specific observed compositions from which the computed curves were inferred. The numbers are the absolute temperatures used to calculate the evaporation curves shown. For each inclusion, the open symbol indicates the pre-evaporation composition, and the filled symbol of the same shape indicates the observed composition. Evaporation curves for E49 and E49A are solid and dashed, respectively.

than for the other Type Bs. First, this is another object for which the observed composition was obtained by INAA. Second, it has an unusual, Mg-rich starting composition whose mineral assemblage was undoubtedly forsterite-rich. There are no existing constraints on evaporation temperatures of such objects, so the selected model temperature, though within the range of those used for other Type Bs, may not be appropriate for this composition.

4.8. Refractory element enrichment factors

For each sample in Fig. 8, the wt% $CaO + Al_2O_3$ is plotted against the wt% $MgO + SiO_2$ for the observed compositions (Table 4) in Fig. 12a and for the pre-evaporation compositions (Table 5) in Fig. 12b. Types A and B inclusions are plotted as filled and open symbols, respectively. The inverse linear correlations are a simple consequence of the fact that these are the only four oxide components considered here. Shown for reference are a series of lines

a

b
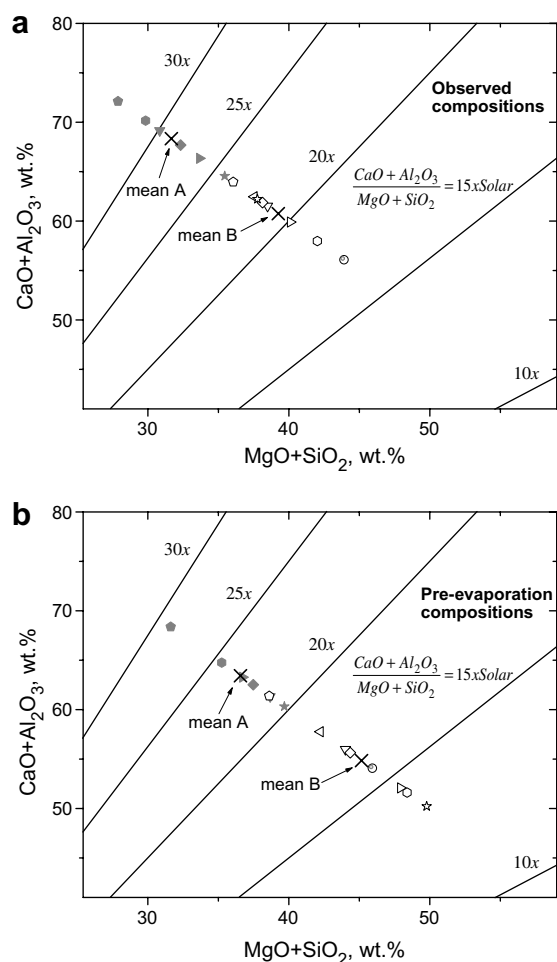
Fig. 12. Observed (a) and pre-evaporation (b) compositions of refractory inclusions are enriched in $CaO + Al_2O_3$ relative to $MgO + SiO_2$ compared to solar abundances. About 80% of the enrichment in $CaO + Al_2O_3$ relative to $MgO + SiO_2$ is due to initial condensation, and 20% is due to subsequent evaporation. Symbols as in Fig. 9.

radiating from the origin whose slopes are equal to the specified multiples of the solar system $(CaO + Al_2O_3)/(MgO + SiO_2)$ ratio of 0.07502. The average observed Types A and B compositions, corrected for non-representative sampling, are plotted on Fig. 12a, and the average pre-evaporation compositions on Fig. 12b.

Among the observed compositions, Type As are enriched in $(CaO + Al_2O_3)/(MgO + SiO_2)$ relative to the solar system abundances by factors of 24–33; Type Bs by factors of 17–24. This is merely a reflection of the higher MgO and SiO_2 contents of Type Bs that was previously noted. For Type As, the average enrichment factor of $(CaO + Al_2O_3)/(MgO + SiO_2)$ is 29.0 relative to the solar system abundances; for Type Bs, it is 20.8.

Among the pre-evaporation compositions, Type As are enriched in $(CaO + Al_2O_3)/(MgO + SiO_2)$ relative to the solar system abundances by factors of 21–29; Type Bs by factors of 13–21. For Type As, the average enrichment factor of $(CaO + Al_2O_3)/(MgO + SiO_2)$ is 23.3 relative to the solar system abundances; for Type Bs, it is 16.4. The lower enrichments in relatively refractory $CaO + Al_2O_3$ compared to relatively volatile $MgO + SiO_2$ in the pre-evaporation compositions compared to the observed compositions is due to removal of the effects of evaporation from the pre-evaporation compositions. Dividing the average enrichment factors for the pre-evaporation compositions by the averages for the observed compositions yields the fraction of the refractory element enrichment due to initial condensation. For Type As, 80.3% of the refractory element enrichment is due to initial condensation and 19.7% due to subsequent evaporation. For Type Bs, the corresponding proportions are 78.9% and 21.2%.

4.9. Implications of inclusions with enrichments in light isotopes

The negative F_{Si} and/or F_{Mg} of the two Type A inclusions, E13 and E62, in Table 4 precludes computation of their pre-evaporation compositions. Such light-isotope enrichments may be due to a kinetic isotope effect accompanying condensation. Why these two objects are the only ones in this study that show this feature is unknown. The size of such an effect may, however, be related to the degree of isotope exchange or back-reaction during evaporation in a closed system. Grossman and Fedkin (2003) presented a model study of chemical and isotopic effects of evaporation of Mg and Si from CMAS liquids into a closed system of solar composition. In cases where evaporation occurred during cooling of the droplet, they found a narrow temperature/time interval for each element within which the flux reversed direction, and evaporation was replaced by condensation with falling temperature. In such circumstances, isotopic exchange led to very large reductions in $\delta^{25}Mg$ of the droplet just before and just after net condensation of Mg began, sometimes even resulting in negative $\delta^{25}Mg$, before a significant increase in the MgO content of the droplet occurred. While the flux reversal occurred at very low Mg concentration in the droplet, an analogous effect might happen at higher Mg content if evaporation occurs in a dust-enriched system. Upon discovering several coarse-grained

inclusions whose Ca was mass-fractionated in favor of light isotopes and whose Mg was mass-fractionated in favor of heavy isotopes, Niederer and Papanastassiou (1984) suggested that the Ca-isotopic composition reflected formation of early condensates while the Mg-isotopic composition recorded an evaporation process.

If a kinetic isotope effect during condensation or back-reaction is the cause of the negative mass-fractionations in E13 and E62, it may have also affected the isotopic compositions of the other CAIs without reducing their F_{Si} or F_{Mg} to negative values. If so, the strategy adopted herein of using the Rayleigh equation to calculate pre-evaporation chemical compositions of inclusions from their F_{Si} and F_{Mg} data would be seriously flawed. If, however, such isotopic exchange had significantly affected the CAIs studied here, it is likely that much greater difficulty would have been encountered in recovering their observed compositions by forward kinetic modeling of pre-evaporation compositions inferred from the Rayleigh equation. Perhaps this is the reason for the relatively poor agreement between model evaporation curves and the observed compositions of E55, E49A and E60.

5. CONCLUSIONS

When the bulk chemical compositions of samples of Types A and B coarse-grained inclusions from CV3 chondrites are corrected for non-representative sampling in the laboratory and then corrected for evaporative losses inferred from their Mg- and Si-isotopic compositions assuming Rayleigh fractionation, the resulting pre-evaporation chemical compositions are consistent with those predicted for high-temperature condensates from equilibrium thermodynamic calculations. To explain all pre-evaporation compositions in this way, however, different inclusions must have condensed from nebular regions differing in total pressure by a factor of 10^5, regardless of whether they formed in a system of solar composition or in one enriched in OC dust relative to gas by a factor of 10 relative to solar composition. The inferred range of total pressure is similar to that predicted by dynamic models of the solar nebula for regions whose temperatures are in the range of silicate condensation temperatures. Alternatively, if departure from equilibrium condensation and/or non-representative sampling of condensates in the nebula occurred, the inferred range of total pressure could be smaller. Simple kinetic modeling of evaporation successfully reproduces observed chemical compositions of most inclusions from their inferred pre-evaporation compositions, suggesting that closed-system isotopic exchange processes did not have a significant effect on their isotopic compositions. Comparison of pre-evaporation compositions with observed ones indicates that 80% of the enrichment in refractory $CaO + Al_2O_3$ relative to more volatile $MgO + SiO_2$ is due to initial condensation and 20% due to subsequent evaporation for both Type A and Type B inclusions.

ACKNOWLEDGMENTS

REFERENCES

Amelin Y., Grossman L., Krot A. N., Pestaj T., Simon S. B. and Ulyanov A. A. (2002) U–Pb age of refractory inclusions from the CV carbonaceous chondrites Allende and Efremovka. *Lunar Planet. Sci.* **XXXIII**, 1151 (abstr.).

Anders E. and Grevesse N. (1989) Abundances of the elements: meteoritic and solar. *Geochim. Cosmochim. Acta* **53**, 197–214.

Berman R. G. (1983). *A Thermodynamic Model for Multicomponent Melts, with Application to the System CaO–MgO–Al₂O₃–SiO₂*. Ph.D. Dissertation, University of British Columbia.

Chou C.-L., Baedecker P. A. and Wasson J. T. (1976) Allende inclusions: volatile-element distribution and evidence for incomplete volatilization of presolar solids. *Geochim. Cosmochim. Acta* **40**, 85–94.

Christophe Michel-Lévy M. (1968) Un chondre exceptionnel dans la météorite de Vigarano. *Bull. Soc. Fr. Minéral. Cristallogr.* **91**, 212–214.

Clayton R. N. and Mayeda T. K. (1963) The use of bromine pentafluoride in the extraction of oxygen from oxides and silicates for isotopic analysis. *Geochim. Cosmochim. Acta* **27**, 43–52.

Clayton R. N. and Mayeda T. K. (1983) Oxygen isotopes in eucrites, shergottites, nakhlites, and chassignites. *Earth Planet. Sci. Lett.* **62**, 1–6.

Clayton R. N., Onuma N., Grossman L. and Mayeda T. K. (1977) Distribution of the pre-solar component in Allende and other carbonaceous chondrites. *Earth Planet. Sci. Lett.* **34**, 209–224.

Clayton R. N., Mayeda T. K., MacPherson G. J. and Grossman L. (1987) Oxygen and silicon isotopes in inclusions and chondrules from Vigarano. *Lunar Planet. Sci.* **XVIII**, 185–186 (abstr.).

Ding T. (2004) Analytical methods for silicon isotope determinations. In *Handbook of Stable Isotope Analytical Techniques*, vol. 1 (ed. P. A. De Groot). Elsevier, Amsterdam, pp. 523–537.

Ding T., Wan D., Bai R., Zhang Z., Shen Y. and Meng R. (2005) Silicon isotope abundance ratios and atomic weights of NBS-28 and other reference materials. *Geochim. Cosmochim. Acta* **69**, 5487–5494.

Dowty E. and Clark J. R. (1973) Crystal structure refinement and optical properties of a Ti³⁺ fassaite from the Allende meteorite. *Am. Mineral.* **58**, 230–242.

Ebel D. S. and Grossman L. (2000) Condensation in dust-enriched systems. *Geochim. Cosmochim. Acta* **64**, 339–366.

Fedkin A. V. and Grossman L. (2006) The fayalite content of chondritic olivine: obstacle to understanding the condensation of rocky material. In *Meteorites and the Early Solar System II* (eds. D. S. Lauretta and H. Y. McSween Jr.). University of Arizona Press, Tucson, AZ, pp. 279–294.

Galy A., Young E. D., Ash R. D. and O'Nions R. K. (2000) The formation of chondrules at high gas pressures in the solar nebula. *Science* **290**, 1751–1753.

Galy A., Belshaw N. S., Halicz L. and O'Nions R. K. (2001) High-precision measurement of magnesium isotopes by multiple-collector inductively coupled plasma mass spectrometry (MC-ICPMS). *Int. J. Mass Spectrosc.* **208**, 89–98.

Galy A., Yoffe O., Janney P. E., Williams R. W., Cloquet C., Alard O., Halicz L., Wadhwa M., Hutcheon I. D., Ramon E. and Carignan J. (2003) Magnesium isotope heterogeneity of the isotopic standard SRM980 and new reference materials for magnesium-isotope-ratio measurements. *J. Anal. At. Spectrom.* **18**, 1352–1356.

Georg R. B., Halliday A. N., Schauble E. A. and Reynolds B. C. (2007) Silicon in the Earth's core. *Nature* **447**, 1102–1106.

Grossman L. (1972) Condensation in the primitive solar nebula. *Geochim. Cosmochim. Acta* **36**, 597–619.

Grossman L. (1980) Refractory inclusions in the Allende meteorite. *Ann. Rev. Earth Planet. Sci.* **8**, 559–608.

Grossman L. and Fedkin A. V. (2003) CaO–MgO–Al₂O₃–SiO₂ liquids: chemical and isotopic effects of Mg and Si evaporation in a closed system of solar composition. *Geochim. Cosmochim. Acta* **67**, 4205–4221.

Grossman L., Ebel D. S., Simon S. B., Davis A. M., Richter F. M. and Parsad N. M. (2000) Major element chemical and isotopic compositions of refractory inclusions in C3 chondrites: the separate roles of condensation and evaporation. *Geochim. Cosmochim. Acta* **64**, 2879–2894.

Grossman L., Ebel D. S. and Simon S. B. (2002) Formation of refractory inclusions by evaporation of condensate precursors. *Geochim. Cosmochim. Acta* **66**, 145–161.

Grossman L., Simon S. B., Rai V. K., Thiemens M. H., Hutcheon I. D., Williams R. W., Galy A., Ding T., Clayton R. N. and Mayeda T. K. (2007) Primordial compositions of refractory inclusions. *Lunar Planet. Sci.* **XXXVIII**, #2172 (abstr.).

Grossman L., Beckett J. R., Fedkin A. V., Simon S. B. and Ciesla F. J. (2008) Redox conditions in the solar nebula: observational, experimental and theoretical constraints. In: *Oxygen in the Solar System* (eds. G. J. MacPherson, D. W. Mittlefehldt, J. H. Jones and S. B. Simon). Rev. Mineral. Geochem., vol. **68**, Mineralogical Society of America, Chantilly, VA, pp. 93–140.

Knight K. B., Davis A. M., Kita N. T., Mendybaev R. A., Richter F. M. and Valley J. W. (2007) Silicon isotope fractionation in CAI-composition evaporation experiments. *Meteorit. Planet. Sci.* **42** (Suppl.), A85 (abstr.).

Loss R. D., Lugmair G. W., MacPherson G. J. and Davis A. M. (1990) Isotope anomalies in Vigarano CAI's-hic et ubique. *Lunar Planet. Sci.* **XXI**, 718–719 (abstr.).

MacPherson G. J. and Davis A. M. (1993) A petrologic and ion microprobe study of a Vigarano Type B refractory inclusion: evolution by multiple stages of alteration and melting. *Geochim. Cosmochim. Acta* **57**, 231–243.

MacPherson G. J., Petaev M. I. and Krot A. N. (2004) Bulk compositions of CAIs and Al-rich chondrules: Implications of the reversal of the anorthite/forsterite condensation sequence at low nebular pressures. *Lunar Planet. Sci.* **XXXV**, #1838 (abstr.).

MacPherson G. J., Simon S. B., Davis A. M., Grossman L. and Krot A. N. (2005) Calcium–aluminum-rich inclusions: major unanswered questions. In: *Chondrites and the Protoplanetary Disk*, ASP Conference Series (eds. A. N. Krot, E. R. D. Scott and B. Reipurth). Astronomical Society of the Pacific, San Francisco, CA, pp. 225–250.

Molini-Velsko, C. (1983) *Isotopic Composition of Silicon in Meteorites*. Ph.D. Dissertation, The University of Chicago.

Molini-Velsko C., Mayeda T. K. and Clayton R. N. (1986) Isotopic composition of silicon in meteorites. *Geochim. Cosmochim. Acta* **50**, 2719–2726.

Niederer F. R. and Papanastassiou D. A. (1984) Ca isotopes in refractory inclusions. *Geochim. Cosmochim. Acta* **48**, 1279–1293.

Notsu K., Onuma N., Nishada N. and Nagasawa H. (1978) High temperature heating of the Allende meteorite. *Geochim. Cosmochim. Acta* **42**, 903–907.

Petaev M. I. and Wood J. A. (1998) The CWPI model of nebular condensation: effects of pressure on the condensation sequence. *Meteorit. Planet. Sci.* **33** (Suppl.), A122 (abstr.).

Prombo C. A. and Lugmair G. W. (1986) Search for correlated isotope effects in Allende CAIs. *Lunar Planet. Sci.* **XVII**, 685–686 (abstr.).

Prombo C. A., Hashimoto A., Birck J. L., Lugmair G. W. and Grossman L. (1987) Search for correlated isotopic effects in Allende CAIs. II. Comparison with mineralogical data. *Lunar Planet. Sci.* **XVIII**, 804–805 (abstr.).

Richter F. M., Davis A. M., Ebel D. S. and Hashimoto A. (2002) Elemental and isotopic fractionation of Type B calcium-, aluminum-rich inclusions: experiments, theoretical considerations, and constraints on their thermal evolution. *Geochim. Cosmochim. Acta* **66**, 521–540.

Richter F. M., Janney P. E., Mendybaev R. A., Davis A. M. and Wadhwa M. (2005) On the temperature dependence of the kinetic isotope fractionation of Type B CAI-like melts during evaporation. *Lunar Planet. Sci.* **XXXVI**, #2124 (abstr.).

Ruden S. P. and Pollack J. B. (1991) The dynamical evolution of the protosolar nebula. *Astrophys. J.* **375**, 740–760.

Simon S. B. and Grossman L. (2004) A preferred method for the determination of bulk compositions of coarse-grained refractory inclusions and some implications of the results. *Geochim. Cosmochim. Acta* **68**, 4237–4248.

Simon S. B., Davis A. M. and Grossman L. (1999) Origin of compact Type A refractory inclusions from CV3 carbonaceous chondrites. *Geochim. Cosmochim. Acta* **63**, 1233–1248.

Simon S. B., Grossman L., Hutcheon I. D., Williams R. W., Galy A., Fedkin A. V., Clayton R. N. and Mayeda T. K. (2004) Determination of primordial refractory inclusion compositions. *Lunar Planet. Sci.* **XXXV**, #1684 (abstr.).

Sylvester P. J., Grossman L. and MacPherson G. J. (1992) Refractory inclusions with unusual chemical compositions from the Vigarano carbonaceous chondrite. *Geochim. Cosmochim. Acta* **56**, 1343–1363.

Tipper E. T., Galy A. and Bickle M. J. (2006) Riverine evidence for a fractionated reservoir of Ca and Mg on the continents: Implications for the oceanic Ca cycle. *Earth Planet. Sci. Lett.* **247**, 267–279.

Wark D. A. and Lovering J. F. (1977) Marker events in the early evolution of the solar system: Evidence from rims on Ca–Al-rich inclusions in carbonaceous chondrites. In *Proc. Lunar Sci. Conf. 8th.* Pergamon Press, NY, pp. 95–112.

Wood J. A. (1967) Olivine and pyroxene compositions in Type II carbonaceous chondrites. *Geochim. Cosmochim. Acta* **31**, 2095–2108.

Yoneda S. and Grossman L. (1995) Condensation of CaO–MgO–Al₂O₃–SiO₂ liquids from cosmic gases. *Geochim. Cosmochim. Acta* **59**, 3413–3444.

Associate editor: Alexander N. Krot